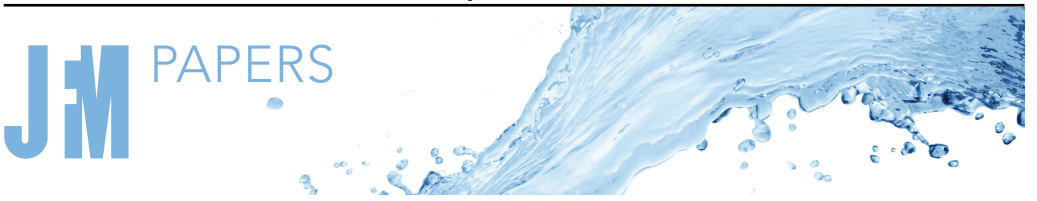
J. Fluid Mech. (2026), *vol.* 1044, A34, doi:10.1017/jfm.2026.12105



Convection in a fluid layer driven by internal dielectric heating

Peter Sebastian Benedek Szabo[1], **Kushal Nagaraj**[1], **Yousuf Ali Mohammed**[1], **Matthias Strangfeld**[1], **Florian Zaussinger**[2] and **Christoph Egbers**[1]

[1]Department of Aerodynamics and Fluid Mechanics, Brandenburg University of Technology Cottbus-Senftenberg, Siemens-Halske-Ring 15a, Cottbus 03046, Germany

[2]Faculty Applied Computer Sciences and Biosciences, Mittweida University of Applied Sciences, Technikumplatz 17, Mittweida 09648, Germany

Corresponding author: Peter Sebastian Benedek Szabo, peter-szabo@gmx.de

(Received 5 March 2026 UTC; revised 24 July 2026 UTC; accepted 30 August 2026 UTC)

This study investigates the convective behaviour of two dielectric fluids with different Prandtl numbers under microgravity, each of which is confined between two parallel electrodes at a given temperature, and subjected to internal dielectric heating. Three-dimensional direct numerical simulations reveal a rich sequence of flow regimes as the electric Rayleigh–Roberts number increases: stable hexagonal patterns, mixed hexagonal-square structures, dominant rectangular convection and time-dependent convection. We derive scaling laws for key dimensionless quantities, including energy densities, convective Reynolds number and Nusselt number, with strong agreement across two magnitudes of the control parameter. Finally, we observe a shift in the onset of convection, with the critical electric Rayleigh–Roberts number increasing as the thermoelectric coupling parameter decreases. These results offer new insights into the role of internal dielectric heating in convective pattern formation and energy transport.

Key words: buoyancy-driven instability, convection in cavities, buoyant boundary layers

1. Introduction

In classical buoyancy-driven flows such as Rayleigh–Bénard convection, fluid motion is primarily governed by gravity and boundary heating. Warmer, less dense fluid ascends, while cooler, denser fluid descends, which is true for fluids without density

© The Author(s), 2026. Published by Cambridge University Press. This is an Open Access article, distributed under the terms of the Creative Commons Attribution licence (https://creativecommons.org/licenses/by/4.0/), which permits unrestricted re-use, distribution and reproduction, provided the original article is properly cited.

https://doi.org/10.1017/jfm.2026.12105 Published online by Cambridge University Press

anomalies. In many natural and industrial systems, heat is not only externally supplied, but instead produced internally within the system. In planetary interiors, radioactive decay and gravitational compression drive mantle convection, influencing plate tectonics, the geomagnetic field, and the thermal and chemical evolution of planetary interiors (McKenzie *et al.* 1973; Schubert *et al.* 2001; Samuel & Farnetani 2003; Ricard 2007; Nakagawa & Tackley 2014). Internal heating (IH) also governs atmospheric convection on Venus (Tritton 1975) and the formation of polygonal terrain on Pluto (Trowbridge *et al.* 2016). An IH fluid can therefore cause buoyancy-driven flows even without boundary heating in the presence of a volumetric body force such as gravity, which can lead to complex flow patterns and instabilities (see Vilella *et al.* 2018).

The dynamics of IH convection is governed by the volumetric heating rate H, and characterised by the Rayleigh–Roberts number R, derived under the Boussinesq (1903) approximation. In other words, for fluid layers, the Rayleigh number Ra is modified by the IH sources, which is related to the temperature difference ΔT (Roberts 1967; Schubert *et al.* 2001), leading to the definition

$$R = \frac{\alpha \Delta T g d^3}{\nu \kappa}, \quad \text{with} \quad \Delta T = \frac{H d^2}{k}, \tag{1.1}$$

where α is the thermal expansion coefficient, g is the gravitational acceleration, d is the layer thickness, ν is the kinematic viscosity, κ is the thermal diffusivity, and k is the thermal conductivity. (The characteristic fluid layer thickness depends on the imposed thermal boundary conditions. For configurations with heating applied only at one boundary, the characteristic length scale is the full layer thickness d. In contrast, when both opposite bounding plates are cooled, the appropriate characteristic length scale is $d/2$; Kulacki & Goldstein 1972; Vilella *et al.* 2018.)

Internally heated convection has been sparsely studied in two main configurations. In the first, IH1, the fluid is uniformly heated with both opposite bounding plates at equally fixed temperatures, explored experimentally by Fiedler & Wille (1970), Kulacki & Goldstein (1972), Kulacki & Nagle (1975), Kulacki & Emara (1977) and Lee *et al.* (2007), and via two-dimensional (2-D) and three-dimensional (3-D) direct numerical simulations (DNS) by McKenzie *et al.* (1973), Emara & Kulacki (1980), Goluskin & Spiegel (2012), Goluskin & van der Poel (2016), Kazemi *et al.* (2022), Arslan *et al.* (2023) and Arslan & Rojas (2025). In the second configuration, IH2, the bottom boundary is insulated, which was studied experimentally by Lee *et al.* (2007), in 2-D DNS by Peckover & Hutchinson (1974), Straus (1976) and Arslan *et al.* (2023), and in 3-D DNS by Wörner *et al.* (1997) and Vilella *et al.* (2018). Rotation in the plane layer has also received recent attention, with analytical bounds (Arslan 2024) and 3-D DNS (Ostilla-Mónico & Arslan 2025).

A common relationship to characterise convection in IH fluids is the volume-averaged temperature T_{vol}, also commonly known as the mean temperature, in contrast to the Rayleigh–Roberts number and the Prandtl number. So far, experiments and DNS have shown a decrease of T_{vol} with increasing R (Kulacki & Goldstein 1972; Goluskin & Spiegel 2012; Goluskin & van der Poel 2016). Wang *et al.* (2021) provided a scaling $T_{vol} \sim R^{-1/5}$ for boundary-layer-dominated regimes, which is consistent with DNS provided by Kazemi *et al.* (2022). For larger Prandtl number or turbulent regimes, a scaling $T_{vol} \sim R^{-1/4}$ is predicted. Rigorous upper bounds on heat transport in IH convection have further been established using variational methods (Arslan *et al.* 2021*a*,*b*; Kumar *et al.* 2022).

In microgravity, as considered in the present study, natural convection is absent. As a result, the flow can only be driven by body force densities other than gravity, such as those generated by electric or magnetic fields to which the fluid responds. The asymmetry

https://doi.org/10.1017/jfm.2026.12105 Published online by Cambridge University Press

between the bounding plates characterising classical IH1 convection therefore vanishes, and heat is transported symmetrically between the two boundaries. The relevant questions therefore concern how the boundary layer (BL) thickness and T_{vol} vary with the Rayleigh–Roberts number and Prandtl number in these systems as a function of the forcing strength.

1.1. *Dielectrophoretic convection*

Since the pioneering work of Senftleben (1932), it has been recognised that electric fields can influence heat transfer in dielectric fluids (Senftleben & Pietzner 1933; Senftleben & Braun 1936). When a polar dielectric fluid is subjected to a high-frequency alternating electric field, permanent molecular dipoles undergo field-driven reorientation. Because this orientational polarisation exhibits a finite relaxation time, the polarisation cannot follow the oscillating field instantaneously, giving rise to a phase lag between the electric field and polarisation. The associated dielectric losses convert electromagnetic energy into volumetric heat, and distribute thermal energy internally. The resulting temperature gradients modify the fluid's electric permittivity, giving rise to an electrohydrodynamic (EHD) body force, which drives convection even in the absence of gravity. This provides a controllable analogue of classical IH convection by utilising dielectric fluids in a microgravity environment. The EHD force density acting on a dielectric fluid is given by

$$\boldsymbol{f}_{EHD} = \rho_e \boldsymbol{E} - \frac{1}{2}\boldsymbol{E}^2\,\nabla\epsilon + \nabla\left[\rho\left(\frac{\partial\epsilon}{\partial\rho}\right)_T \frac{\boldsymbol{E}^2}{2}\right], \tag{1.2}$$

where ρ_e is the density of free electric charge, $\boldsymbol{E}$ is the electric field, ρ is the fluid density, ϵ is the electric permittivity, and T is the temperature (Landau *et al.* 1984). The three terms on the right-hand side represent the electrophoretic (Coulomb), dielectrophoretic (DEP) and electrostrictive force densities, respectively. At small frequencies, the Coulomb force density on free charges dominates the flow dynamics, even in initially electroneutral media. To ensure that charge-related effects remain negligible, the field frequency must satisfy

$$\omega \gg \tau_e^{-1}, \tau_\nu^{-1}, \tau_\kappa^{-1}, \tau_m^{-1}, \tau_d^{-1}, \tag{1.3}$$

where ω is the angular frequency of the applied alternating electric field. This high-frequency condition states, with the characteristic time scales of charge relaxation τ_e, viscous dissipation τ_ν, thermal diffusion τ_κ, ion migration τ_m and mass diffusion τ_d, that a dielectric fluid is unable to respond dynamically, and the resulting Coulomb force density cancels out over a period of the electric field variation. The remaining forces are the DEP force density and the electrostrictive force density, as both have non-zero time average because of $\boldsymbol{E}^2$ and the time-averaged dielectric heating rate H (see Yoshikawa *et al.* 2020). In the absence of mobile boundaries, the electrostrictive force has no effect on the motion of an incompressible fluid, which is considered for the particular working fluid (see Turnbull 1968; Jones 1979; Yoshikawa *et al.* 2013*b*). The remaining force is due to the DEP force density, which depends on the temperature-sensitive permittivity $\epsilon(T)$, and varies among dielectric fluids. In most cases, it decreases with increasing temperature. For the majority of fluids, $\epsilon(T)$ can be approximated by the equation of state written as

$$\epsilon(T) = \epsilon_0\epsilon_r\,[1 - e\,(T - T_0)], \tag{1.4}$$

where $\epsilon_0 = 8.854 \times 10^{-12}\ \mathrm{F\,m^{-1}}$ is the vacuum permittivity, ϵ_r is the relative permittivity, $e = -(1/\epsilon_r)\,\partial\epsilon_r/\partial T$ is the thermal permittivity coefficient (typically 10^{-3}–$10^{-1}\ \mathrm{K^{-1}}$), and T_0 is the reference temperature where the fluid parameters are defined (see Yoshikawa *et al.* 2013*b*; Mutabazi *et al.* 2016; Szabo & Egbers 2025).

https://doi.org/10.1017/jfm.2026.12105 Published online by Cambridge University Press

To isolate the DEP force density from Archimedean buoyancy, many experiments are conducted under microgravity. The arising convective phenomenon is known as thermoelectrohydrodynamic (TEHD) convection. This particular kind of convection in an incompressible dielectric fluid has been studied in planar fluid layers (see Turnbull 1968; Roberts 1969; Takashima 1976; Stiles 1991; Yoshikawa *et al.* 2013*b*; Barry *et al.* 2023) and cylindrical annuli (see Takashima 1980; Yavorskaya *et al.* 1984; Yoshikawa *et al.* 2013*a*; Travnikov *et al.* 2015, 2016; Meier *et al.* 2018; Szabo *et al.* 2021, 2022, 2023; Kang *et al.* 2024), which are more relevant to heat transfer enhancement considering applications such as in a heat exchanger. The influence of the DEP force density has also been investigated in spherical geometries, primarily to model large-scale geophysical flows (see Chandra & Smylie 1972; Hart *et al.* 1986; Beltrame *et al.* 2003; Egbers *et al.* 2003; Travnikov *et al.* 2003; Zaussinger *et al.* 2020; Travnikov & Egbers 2021). A pioneering geophysical experiment proposed by Chandra & Smylie (1972) and later realised by Hart *et al.* (1986) evolved into the GeoFlow series aboard the International Space Station (see Beltrame *et al.* 2003; Egbers *et al.* 2003; Travnikov *et al.* 2003; Zaussinger *et al.* 2020; Travnikov & Egbers 2021), where a central force field in a spherical shell simulated mantle–core flow. The flow dynamics, visualised via Wollaston shearing interferometry, was validated against numerical models (see Futterer *et al.* 2010, 2013; Zaussinger *et al.* 2017). A follow-up experiment, AtmoFlow, is currently in preparation (see Travnikov & Egbers 2021; Gaillard *et al.* 2024, 2025; Travnikov *et al.* 2025; Gaillard *et al.* 2026), which aims to investigate planetary atmospheres. For a broader discussion of TEHD convection, the reader is referred to the review by Mutabazi *et al.* (2016), which provides a detailed overview of the onset of TEHD convection in different geometries, and discusses the electric Rayleigh number, a key non-dimensional parameter originally introduced by Turnbull (1968) and Roberts (1969).

1.2. *Convection in internally dielectric heated fluids*

Most prior studies have focused on perfect dielectric fluids and neglected dielectric losses, thereby excluding IH terms from the energy equation. Only a few experiments involving polar fluids in spherical geometries have considered these losses explicitly (see Travnikov *et al.* 2020; Zaussinger *et al.* 2020; Travnikov & Egbers 2021). A recent study by Yoshikawa *et al.* (2020) investigated TEHD convection in a plane capacitor under microgravity and terrestrial conditions, using a dielectric fluid heated via dielectric loss between bounding plates. In this context, the electric Rayleigh number was reformulated to account for electric field effects and dielectric heating, yielding a form analogous to the Rayleigh–Roberts number introduced in (1.1). A crucial parameter for the study was the thermoelectric coupling parameter γ_e, which accounts for electric field variations in Gauss's law related to the temperature-dependent electric permittivity defined in (1.4). This parameter is dependent on the used dielectric fluid and the caused dielectric losses that induce temperature gradients throughout the fluid (see Yoshikawa *et al.* 2013*b*). For the onset of convection, γ_e is relevant; however, it increases with ΔT for values above the onset.

1.3. *Aim and objectives*

The present work investigates TEHD convection in internal dielectric heated polar fluids, extending the parameter space of the numerical simulations by Yoshikawa *et al.* (2020) using an alcohol-based fluid (1-Nonanol) and a fluorinated based fluid (Novec 7200), with fluid properties listed in table 2 in Appendix A. We investigate the flow structures and dynamics of a fluid layer subjected to internal dielectric heating and cooled from

https://doi.org/10.1017/jfm.2026.12105 Published online by Cambridge University Press

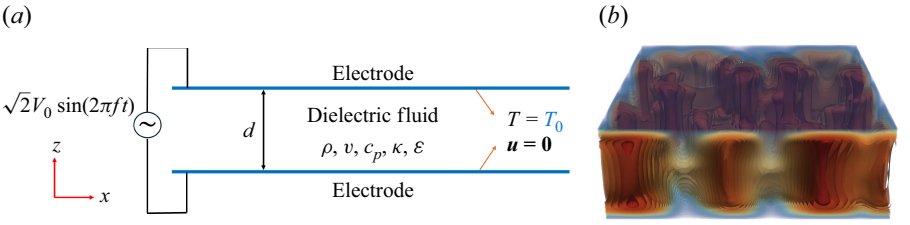


Figure 1. (*a*) Schematic of the problem geometry. (*b*) A representative 3-D temperature field of the numerical data presented in figure 2(*d*).

opposite bounding plates, defined earlier as IH1, in the absence of gravity, following the configuration of Yoshikawa *et al.* (2020). Using DNS, we compare the resulting behaviour with that of conventionally IH fluids, such as those studied by Goluskin (2016) and Vilella *et al.* (2018).

2. Model formulation

2.1. *Problem geometry*

The system investigated consists of a dielectric fluid layer of height d, laterally with periodic conditions, subjected to constant uniform temperature of the bounding plates in space and time. The length and width of the fluid layer are equal, and are a multiple of four times the extracted wavelength found in Yoshikawa *et al.* (2020). No-slip velocity conditions are imposed at both bounding plates. An alternating electric tension $V(t)$ is applied between the bounding plates, whereas one of the bounding plate is grounded. The influence of the resulting electric field on fluid flow and heat transfer is investigated by varying the applied electric tension causing the fluid to heat and investigating two different dielectric loss factors that have been measured for both fluids for an alternating frequency of 50 Hz and 10 kHz. A schematic of the configuration is shown in figure 1.

2.2. *Governing equations*

The high-frequency condition in (1.3) ensures that the fluid remains initially electroneutral, preventing space charge accumulation ($\rho_e = 0$) throughout the development of the convective flow. When the condition $d \gg \lambda_D$ is satisfied, where λ_D is the Debye length, the convective transport of charge from the diffuse layer into the bulk is negligible (see Yoshikawa *et al.* 2013*b*). Under these assumptions, the fluid motion in a dielectric layer can be described using the continuity, momentum and energy equations together with Gauss's law and the EHD Boussinesq approximation, given in (1.4) and read as

$$\boldsymbol{\nabla} \cdot \boldsymbol{u} = 0, \tag{2.1}$$

$$\partial_t \boldsymbol{u} + (\boldsymbol{u} \cdot \boldsymbol{\nabla})\boldsymbol{u} = -\frac{1}{\rho}\boldsymbol{\nabla} P + \nu\, \nabla^2 \boldsymbol{u} + \frac{1}{\rho}\boldsymbol{f}_{DEP}, \tag{2.2}$$

$$\partial_t T + (\boldsymbol{u} \cdot \boldsymbol{\nabla})T = \kappa\, \nabla^2 T + H, \tag{2.3}$$

$$\boldsymbol{\nabla} \cdot [\epsilon(T)\, \boldsymbol{E}] = 0, \quad \text{with} \quad \boldsymbol{E} = -\boldsymbol{\nabla}\phi, \tag{2.4}$$

where $\boldsymbol{u}$ is the velocity field, ϕ is the electric potential, and $\boldsymbol{f}_{DEP}$ is the DEP force density. The generalised EHD Boussinesq approximation states that all thermophysical properties are kept constant except for the electrical permittivity in Gauss's law and in the DEP

https://doi.org/10.1017/jfm.2026.12105 Published online by Cambridge University Press

force density term. This exception is necessary because gradients of electrical permittivity constitute the leading-order mechanism responsible for electrothermal forcing. In the present configuration, the electric-field inhomogeneity is not imposed geometrically, e.g. by curvature, but arises from temperature-induced variations of the electrical permittivity, which generate spatial variations of the electric field and consequently the DEP forcing (see Yoshikawa *et al.* 2020). The modified pressure P is defined by

$$P = p - \frac{1}{2}\rho \left(\frac{\partial \epsilon}{\partial \rho}\right)_T \boldsymbol{E}^2, \tag{2.5}$$

which incorporates the electrostrictive contribution, given by the third term in (1.2), which does not influence the fluid motion if the fluid is incompressible and has no mobile boundaries.

Assuming a sinusoidal electric tension $V(t) = \sqrt{2}V_0 \sin(2\pi f t)$, its root mean square value is defined as $V_0 = \sqrt{\langle V^2(t)\rangle_t}$, where $\langle\cdot\rangle_t$ denotes time averaging over one oscillation period. The time-averaged DEP approximation can be traced back to a parametric study on the validity of TEHD convection, where the condition $2\pi f \tau_v \gtrsim 100$ was identified as a key criterion (Smorodin & Velarde 2001; Yoshikawa *et al.* 2020). Experiments have been conducted within an electrical frequency range of approximately 10^2–10^4 Hz, thereby satisfying this requirement and ensuring the applicability of the approximation (see Turnbull 1969; Chandra & Smylie 1972; Hart *et al.* 1986; Futterer *et al.* 2013; Yoshikawa *et al.* 2020; Szabo *et al.* 2021). Consequently, the time-averaged DEP force density, accounting for the temperature dependence of the permittivity (see (1.4)), becomes

$$\boldsymbol{f}_{DEP} = -\frac{1}{2}\boldsymbol{E}^2\,\boldsymbol{\nabla}\epsilon(T) = \frac{\epsilon_0 \epsilon_r e}{2}\,|-\boldsymbol{\nabla}\phi|^2\,\boldsymbol{\nabla}T, \tag{2.6}$$

where the electric field is expressed as $\boldsymbol{E} = -\boldsymbol{\nabla}\phi$ based on the time-averaged electric potential.

The dielectric loss of the working fluid is given by the loss factor and calculated from the ratio between the dissipative and reactive components of the complex electrical permittivity, written as

$$\text{loss factor} \equiv \tan\delta = \frac{\omega\epsilon'' + \sigma}{\omega\epsilon'}, \tag{2.7}$$

where ϵ' and ϵ'' are the real and imaginary parts of the complex electrical permittivity, $\epsilon = \epsilon' - \mathrm{i}\epsilon''$, with $\mathrm{i} = \sqrt{-1}$. The parameter δ is the dielectric loss angle, and σ is the electrical conductivity. The volumetric heating rate for a dielectrically heated fluid, H, can be defined by

$$H = \frac{\omega \tan\delta\, \epsilon_0 \epsilon_r}{\rho c_p}\boldsymbol{E}^{\boldsymbol{2}} \tag{2.8}$$

and is consistent with Travnikov *et al.* (2020), Zaussinger *et al.* (2020) and Travnikov & Egbers (2021). The respective temperature increase related to dielectric heating can be defined by the equilibrium between the heating power and the thermal diffusion, and can be estimated by

$$\Delta T = \frac{\omega \tan\delta\, \epsilon_0 \epsilon_r V_0^2}{8k}, \tag{2.9}$$

https://doi.org/10.1017/jfm.2026.12105 Published online by Cambridge University Press

and its variation in the electrical permittivity by the dimensionless thermoelectric parameter $\gamma_e = (\epsilon/(\epsilon_0\epsilon_r)) - 1$ by

$$\gamma_e = e\Delta T = \frac{\omega \tan\delta \; e\epsilon_0\epsilon_r V_0^2}{8k}, \tag{2.10}$$

which is consistent with the assumption by Yoshikawa *et al.* (2020), by considering the half-gap distance $d/2$ as the characteristic length scale, as the temperature variation predominantly occurs across this region within the dielectric fluid layer, which is defined as the IH1 configuration.

The governing equations (2.1)–(2.4), including the DEP force density given in (2.6), can be non-dimensionalised using appropriate reference scales. For convection-driven flows, the characteristic thermal time scale d^2/κ is employed. Introducing the following non-dimensional variables,

$$\begin{aligned} &\boldsymbol{u}^* = \boldsymbol{u}\frac{d}{\kappa}, \quad t^* = t\frac{\kappa}{d^2}, \quad \nabla^* = d\,\boldsymbol{\nabla}, \\ &P^* = P\frac{d^2}{\rho\kappa^2}, \quad T^* = \frac{T - T_0}{\Delta T}, \quad \boldsymbol{E}^* = \boldsymbol{E}\frac{d}{V_0}, \end{aligned} \tag{2.11}$$

the conservation equations can be expressed in non-dimensional form, without asterisks, by

$$\boldsymbol{\nabla}\cdot\boldsymbol{u} = 0, \tag{2.12}$$

$$Pr^{-1}\big[\partial_t\boldsymbol{u} + (\boldsymbol{u}\cdot\boldsymbol{\nabla})\boldsymbol{u}\big] = -Pr^{-1}\,\boldsymbol{\nabla}P + \boldsymbol{\nabla}^2\boldsymbol{u} + 2\,\gamma_e^{-1}R_E\boldsymbol{E}^2\boldsymbol{\nabla}T, \tag{2.13}$$

$$\partial_t T + (\boldsymbol{u}\cdot\boldsymbol{\nabla})T = \boldsymbol{\nabla}^2 T + 8\boldsymbol{E}^2, \tag{2.14}$$

$$\boldsymbol{\nabla}\cdot\big[(1-\gamma_e T)\,\boldsymbol{E}\big] = 0, \quad \text{with} \quad \boldsymbol{E} = -\boldsymbol{\nabla}\vartheta, \tag{2.15}$$

where ϑ is the non-dimensional electric potential, and Pr is the Prandtl number given by the dissipation time scale ratio τ_κ/τ_ν. These conservation equations describe electrothermally driven convection, where fluid motion is forced by temperature-induced variations in the dielectric permittivity rather than by gravity as in Rayleigh–Bénard convection. Temperature fluctuations evolve according to (2.14), modify the electric field via (2.15), and generate the body force $2\,\gamma_e^{-1}R_E\,\boldsymbol{E}^2\,\boldsymbol{\nabla}T$ that drives the momentum equation (2.13).

To account for electric forcing, the Rayleigh–Roberts number is reformulated by replacing the temperature difference and gravity in (1.1) with (2.9) and the electric gravity, which reads $g_{e,0} = 2e\epsilon_r\epsilon_0\gamma_e V_0^2/(\rho\alpha d^3)$, respectively (see Yoshikawa *et al.* 2020). This results in an electric Rayleigh–Roberts number given by

$$R_E = \frac{\alpha\Delta T g_{e,0}}{\nu\kappa}\left(\frac{d}{2}\right)^3 = \frac{(\omega\tan\delta)^2 e^2(\epsilon_0\epsilon_r)^3 V_0^6}{256\rho\nu\kappa k^2} = \frac{1}{4}\gamma_e^2 V_E^2, \tag{2.16}$$

where

$$V_E = V_0/\sqrt{\rho\nu\kappa/(\epsilon_0\epsilon_r)} \tag{2.17}$$

is the non-dimensional effective electric potential. Note that V_E depends on fluid properties and can vary significantly between different dielectric liquids such as hydrofluoroethers and alcohols (see Szabo & Egbers 2025).

https://doi.org/10.1017/jfm.2026.12105 Published online by Cambridge University Press

3. Computational methodology

3.1. *Numerical input, schemes and solvers*

The governing equations are solved using a finite-volume formulation implemented in the open-source software package OpenFOAM v2012. The problem geometry shown in figure 1 is subjected to the boundary conditions

$$\begin{cases} \boldsymbol{u} = \boldsymbol{0}, \ T = 0, \ \vartheta = 1 & \text{at} \quad z = 1, \\ \boldsymbol{u} = \boldsymbol{0}, \ T = 0, \ \vartheta = 0 & \text{at} \quad z = 0, \end{cases} \tag{3.1}$$

and solved via a custom-developed `buoyantPimpleFoam` solver developed by (Gaillard *et al.* 2024, 2025). The numerical solution proceeds in two stages: first, the electrostatic and thermal base state is obtained by solving Gauss's law and the energy equation. This solution is then used to initialise the fully coupled, time-dependent simulation of the electric, thermal and flow fields. Further details regarding spatial and temporal discretisation, linear solvers and algorithmic implementation are provided in Appendix B.

3.2. *Parameter choice*

Two dielectric fluids, 1-Nonanol and Novec 7200, are selected due to their contrasting dielectric loss factors, which result in significantly different volumetric heating rates. These fluids also differ in Prandtl number, and have previously been used to study heat transfer enhancement by Yoshikawa *et al.* (2020), and in modelling geophysical and astrophysical flows at laboratory scale (see Zaussinger *et al.* 2020; Travnikov & Egbers 2021).

The volumetric heating rate H depends on the dielectric loss factor $\tan\delta$, angular frequency ω, and applied electric tension V. We experimentally measured $\tan\delta$ at two frequencies, and varied V to define a parameter space suitable for physical experiments, such as those in planar cavities studied by Strangfeld *et al.* (2022) and Szabo & Egbers (2025). To facilitate comparisons with numerical simulations and experiments involving additional gravitational forcing, we use the dimensionless effective electric potential V_E instead of the electric Rayleigh–Roberts number. This choice avoids coupling complications between an arbitrarily selected electric Rayleigh–Roberts number and the Rayleigh number given e.g. in equations (20) and (21) in Yoshikawa *et al.* (2020). This ensures reproducibility in both simulations and experiments by directly mapping V_E to a unique fluid and heating condition.

The parameter space is based on a prior conducted 2-D numerical parametric sweep to investigate the nature of the flow and the evolving convective patterns. For the 3-D numerical simulations, the values of V_E could then be chosen and ranged for 1-Nonanol from 1400 to 3000, while for Novec 7200 the range was 6000–11 000. Simulations were carried out with the two frequencies 50 Hz and 10 kHz, where fluid parameters are known by physical measurements. Using the fluid properties and measured loss factors listed in table 2, the corresponding forcing parameters were calculated (see table 1), which define the parameter space explored in the present study. To get an indication of the parameter space in relation to γ_e, R_E and V_E, the relationships between their individual strengths can be plotted using (2.10), (2.16) and (2.17), respectively.

3.3. *Diagnostics*

To assess the influence of the chosen parameter space on convective and thermal transport, we introduce several diagnostic measures. Volume-averaged quantities are denoted by angle brackets $\langle\cdot\rangle_V$, and overbars $\overline{\ldots}$ indicate temporal averages. The intensity of

https://doi.org/10.1017/jfm.2026.12105 Published online by Cambridge University Press

1-Nonanol					Novec 7200				
V_E	$R_E^{50\,\mathrm{Hz}}$	$\gamma_e^{50\,\mathrm{Hz}}$	$R_E^{10\,\mathrm{kHz}}$	$\gamma_e^{10\,\mathrm{kHz}}$	V_E	$R_E^{50\,\mathrm{Hz}}$	$\gamma_e^{50\,\mathrm{Hz}}$	$R_E^{10\,\mathrm{kHz}}$	$\gamma_e^{10\,\mathrm{kHz}}$
1400	1095.83	0.048	1503.06	0.056	6000	1422.45	0.013	2364.84	0.016
1500	1657.76	0.055	2273.82	0.064	7000	3586.90	0.017	5963.24	0.022
1600	2441.71	0.062	3349.11	0.073	8000	7992.28	0.022	13 287.21	0.029
1900	6846.93	0.088	9391.41	0.102	9000	16 202.65	0.028	26 936.98	0.037
2000	9314.39	0.097	12 775.83	0.113	10 000	30 488.14	0.035	50 686.69	0.046
2250	18 882.94	0.123	25 900.28	0.144	11 000	54 011.61	0.042	89 794.56	0.055
2500	35 531.58	0.151	48 735.94	0.177	—	—	—	—	—
3000	106 096.72	0.218	145 524.73	0.255	—	—	—	—	—

Table 1. Overview of the parameter choice for both working fluids, 1-Nonanol and Novec 7200, at 50 Hz and 10 kHz.

Property	Symbol	Novec 7200	1-Nonanol	Units
Kinematic viscosity	ν	0.471	13.970	$10^{-6}\,\mathrm{m^2\,s^{-1}}$
Density	ρ	1420.000	828.160	$\mathrm{kg\,m^{-3}}$
Thermal expansion coeff.	α	1.605	0.823	$10^{-3}\,\mathrm{K^{-1}}$
Thermal permittivity coeff.	e	2.407	10.209	$10^{-3}\,\mathrm{K^{-1}}$
Electric permittivity (relative)	ϵ_r	7.393	9.056	–
Dielectric loss factor (50 Hz)	$\tan\delta$	8.570	10.660	—
Dielectric loss factor (10 kHz)	$\tan\delta$	5.525	6.242	10^{-2}
Thermal diffusivity	κ	4.510	7.940	$10^{-8}\,\mathrm{m^2\,s^{-1}}$
Thermal conductivity	k	0.070	0.163	$\mathrm{W\,K^{-1}\ m^{-1}}$
Reference temperature	T_0	298.000	293.000	K
Heat capacity	c_p	1092.000	2474.000	$\mathrm{J\,kg^{-1}\,K^{-1}}$
Thermal dissipation time scale	τ_κ	53.100	1.790	s
Viscous dissipation time scale	τ_ν	553.840	314.861	s
Charge relaxation time scale	τ_ϵ	3.716	2.988	s
Characteristic length	d	5.000	5.000	$10^{-3}\,\mathrm{m}$
Prandtl number	Pr	10.430	175.945	—

Table 2. Fluid properties of Novec 7200 and 1-Nonanol.

convection is characterised by the dimensionless kinetic energy density $\tilde{E}_K$, which reflects the strength of advective heat transport over time. The corresponding non-dimensional volume-averaged temperature T_{vol} provides an indication of how well heat is diffused in the overall fluid layer. These quantities are defined as

$$\tilde{E}_K = \frac{1}{2}\,\overline{\langle|\boldsymbol{u}|^2\rangle_V}, \quad T_{vol} = \langle\overline{T}\rangle_V, \tag{3.2}$$

where spatial averaging is performed first, followed by temporal averaging across the entire domain after the flow has equilibrated from the initial state for $\tilde{E}_K$, and vice versa for T_{vol}.

The overall heat transfer enhancement is characterised by the Nusselt number. We consider the IH1 formulation by Goluskin (2016) given by

$$Nu_H = \frac{q_w}{T_{max} - T_w}\frac{d}{4k} = \frac{\left|\partial T/\partial z\right|_w}{T_{max} - T_w}\frac{d}{4}, \tag{3.3}$$

https://doi.org/10.1017/jfm.2026.12105 Published online by Cambridge University Press

where q_w is the conductive flux through one of the boundary plates, with $T_{max} - T_w$ defined as the maximum temperature difference measured across the fluid layer. A value $Nu_H = 1$ represents pure conduction, and $Nu_H > 1$ reflects convective heat transfer in IH1 fluids (Kulacki & Goldstein 1972; Goluskin 2016).

In laboratory settings where gravity is present, Archimedean buoyancy can drive convection in non-isothermal fluids, thereby modifying the energy transport within the system. As a result, heat may be dissipated unevenly between both bounding plates; see e.g. figure 2 in Kulacki & Goldstein (1972). In this study, as indicated by the conservation equation, we examine the IH1 configuration in the absence of gravity.

3.4. *Validation and numerical resolution*

The solver has been extensively validated in previous studies for both natural and TEHD convection, showing deviations of less than 1 % relative to pseudo-spectral and finite-element benchmarks (Gaillard *et al.* 2024, 2025). For the present fluid-layer configuration, additional benchmark comparisons are performed against the reference solutions of Barry *et al.* (2023). Excellent agreement is obtained across the full parameter range, including at high Rayleigh numbers, with discrepancies remaining below 1 % (see figure 10(*a*) below). Mesh-independence tests confirm that all results reported here are numerically converged. Further details of the benchmark configuration and grid-resolution study are provided in Appendix C.

4. Results

This section presents the observed convective structures, which are characterised by their convective morphology. We analyse temperature and velocity profiles, and relate the imposed thermal forcing to the thermal and kinetic BL thicknesses, and energy dissipation in the BL and the bulk of the fluid. The kinetic energy and volume-averaged temperature are discussed, together with the heat transfer quantified by the Nusselt number with respect to the applied forcing.

4.1. *Visualisation and characterisation of observed convective morphology*

The characterisation of convective patterns is based on the temporal evolution and spatial organisation of flow structures. Figure 2 shows iso-surface snapshots of the temperature field T projected along the x, y and z directions, after the system has reached a stationary or quasi-stationary state. The simulations reveal time-invariant plumes shown in figures 2(*a–c*), and time-dependent convection depicted in figure 2(*d*). Four distinct regimes can be classified: at small effective voltage $V_E = 1500$, the plumes form hexagonal patterns evident in the z projection, as seen in figure 2(*a*), but are obscured in the x and y directions due to their oblique orientation. Increasing V_E to 1600 as shown in figure 2(*b*) results in a mixed state of hexagonal and rectangular patterns, with a higher plume density. The section-averaged fields indicate emerging structures in the y direction, while the x direction remains patternless due to obliqueness. With an additional increase to $V_E = 2500$ given in figure 2(*c*), plumes align along the x and y axes, forming well-defined rectangular patterns visible in all projections. At $V_E = 3000$, shown in figure 2(*d*), the flow becomes time-dependent, indicative of deep convection.

4.2. *Mean temperature and velocity profiles*

To obtain temporally and spatially averaged temperature and velocity profiles, we first perform a temporal average for each grid point, followed by sectional averaging in the x

https://doi.org/10.1017/jfm.2026.12105 Published online by Cambridge University Press

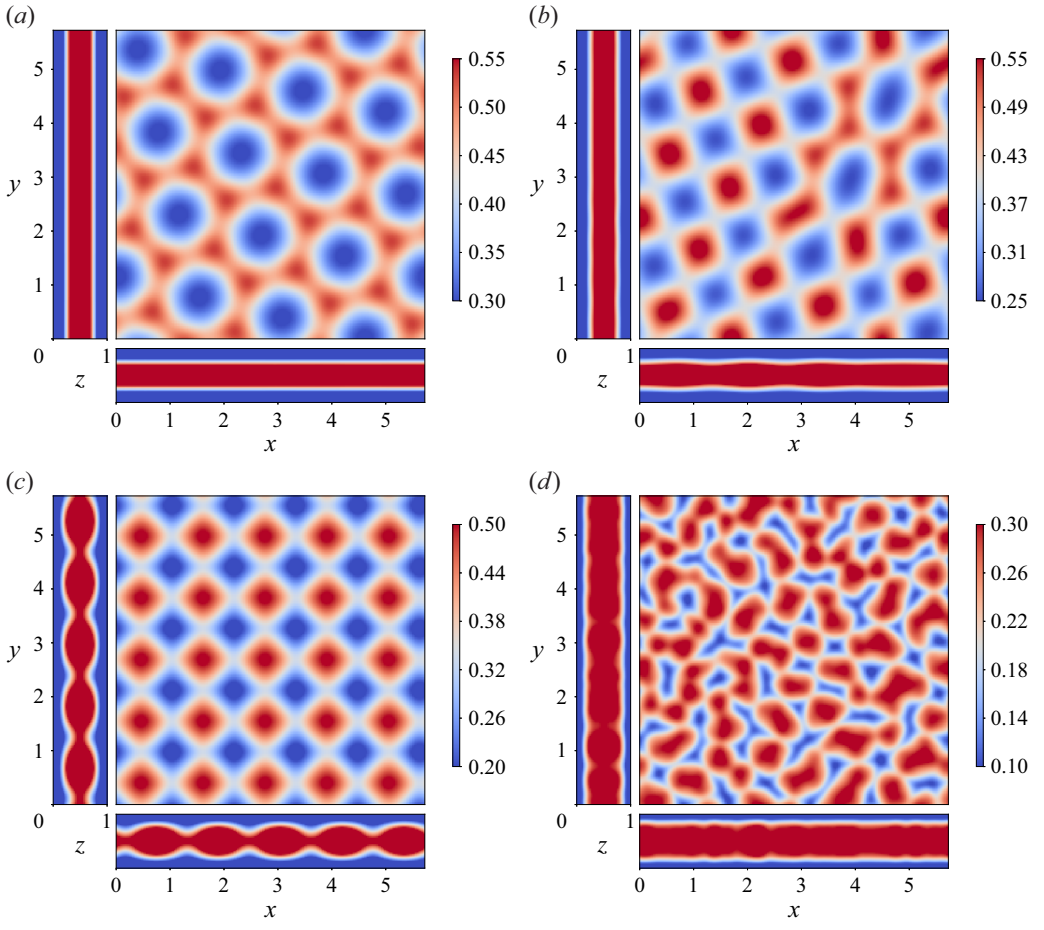


Figure 2. Iso-surfaces of the non-dimensional temperature T projected along the x, y and z directions of 1-Nonanol at 50 Hz: (*a*) $V_E = 1500$ ($R_E = 1657$), (*b*) $V_E = 1600$ ($R_E = 2441$), (*c*) $V_E = 1900$ ($R_E = 6846$), (*d*) $V_E = 3000$ ($R_E = 106\,096$).

direction and then in the y direction over the entire fluid layer. The resulting profiles, denoted as $\langle \overline{T} \rangle_S(z)$ for temperature, and $\langle \overline{U} \rangle_S(z)$ for velocity magnitude denoted by $U = |\boldsymbol{u}|$, characterise the mean behaviour throughout the fluid bulk. The overbar $\overline{\dots}$ represents temporal averaging, and $\langle \cdot \rangle_S$ denotes spatial averaging over the respective cross-sectional plane S, which is consistent with the notation introduced in the diagnostics subsection (§ 3.3). Figure 3 depicts representative profiles of temperature and velocity between the bounding plates for selected values of effective voltage V_E, spanning the explored range of both working fluids and dielectric loss factors.

In all cases, the temperature profile, given in figures 3(*a–d*), rises from one bounding plate to mid-depth ($z = d/2$), then decreases towards the other bounding plate, indicating internal dielectric heating with heat dissipated symmetrically towards both cooled boundaries. For small V_E, the profile is approximately parabolic and extends throughout the bulk, reflecting a thick thermal BL. As V_E increases, the profile flattens near the centre and steepens near the boundaries, indicating the development of thinner thermal BLs. While the profiles remain symmetric, they deviate from the parabolic shape observed at low V_E. The steep gradients near the boundaries indicate a reduction in BL thickness,

https://doi.org/10.1017/jfm.2026.12105 Published online by Cambridge University Press

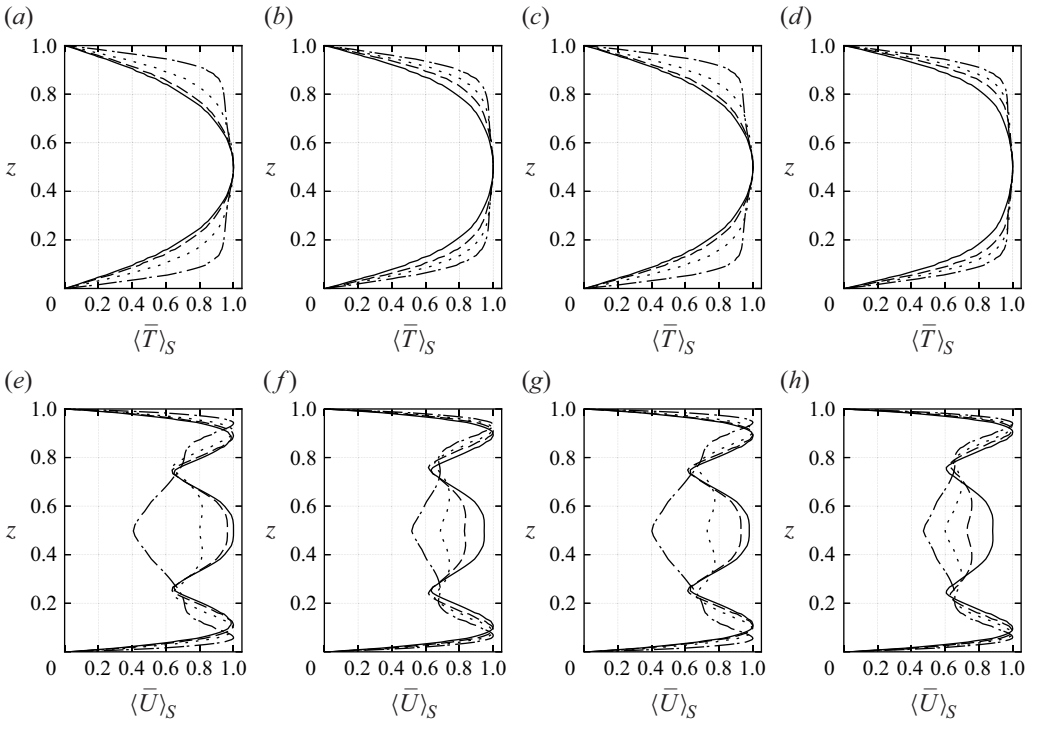


Figure 3. Time- and section-averaged (*a–d*) temperature profiles $\langle\overline{T}\rangle_S(z)$ and (*e–h*) velocity profiles $\langle\overline{U}\rangle_S(z)$, for four cases: (*a*,*e*) 1-Nonanol at 50 Hz, (*b*,*f*) Novec 7200 at 50 Hz, (*c*,*g*) 1-Nonanol at 10 kHz, and (*d*,*h*) Novec 7200 at 10 kHz. For each fluid, results are shown for selected forcing amplitudes: $V_E = 1500$ and 7000 (solid line), $V_E = 1600$ and 8000 (dashed line), $V_E = 1900$ and 9000 (dotted line), and $V_E = 3000$ and 11 000 (dash-dotted line), for 1-Nonanol and Novec 7200, respectively, in the corresponding panels.

consistent with previous studies (see Parmentier & Sotin 2000; Moore 2008; Vilella *et al.* 2018). This is supported by a decreasing trend in the temperature gradient $\partial\langle\overline{T}\rangle_S/\partial z$ near both boundaries with increasing V_E. Additionally, the differing magnitudes of V_E required to achieve similar flow regimes in the two working fluids (1-Nonanol and Novec 7200) reflect the dependence of V_E on the fluid properties, as discussed in § 2.2.

The velocity profile, shown in figures 3(*e–h*), exhibits a more intricate structure. Near both no-slip boundaries, a step increase in velocity is observed, resulting in local maxima that diminish near one-quarter of the fluid depth ($z = d/4$). For small values of V_E, a secondary peak emerges at mid-depth ($z = d/2$), indicating the presence of symmetric convective motions across the layer. This profile suggests the formation of convective rolls extending from each boundary towards the interior. As the forcing increases, the step height at the boundaries becomes more pronounced, while the mid-depth peak changes from a maximum to a minimum, reflecting enhanced outward advection of hot fluid, and intensified convective transport towards the cooler boundaries.

4.3. *The BL development and energy dissipation*

The BLs adjacent to the cooled walls play a crucial role in determining the flow and heat transfer dynamics. The thicknesses of the thermal and kinetic BLs are estimated using the slope method, and are denoted by δ_T and δ_u, respectively. The definitions of the thermal and kinetic BL thicknesses are provided in Appendix D. To examine the BL thicknesses

https://doi.org/10.1017/jfm.2026.12105 Published online by Cambridge University Press

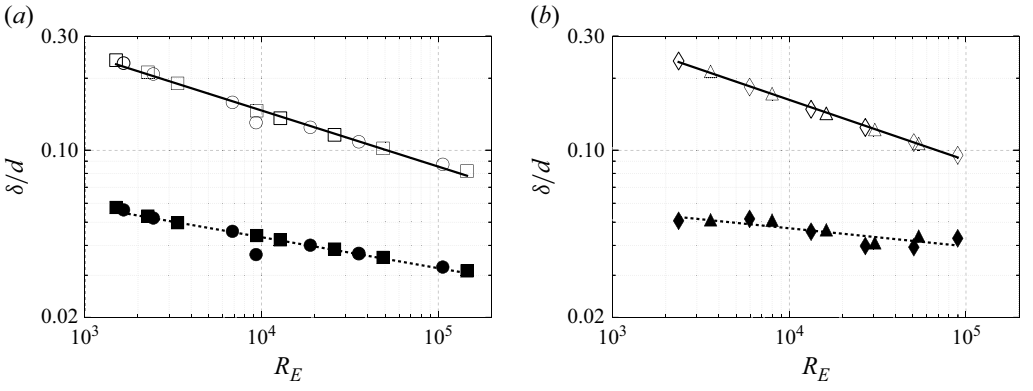


Figure 4. Thermal and kinetic BL thicknesses, normalised by the fluid layer height d (δ_T/d and δ_u/d), plotted versus the electric Rayleigh–Roberts number R_E. (*a*) The markers ○ and □ denote thermal BL thicknesses, and • and ■ denote kinetic BL thicknesses for 1-Nonanol at 50 Hz and 10 kHz, respectively. (*b*) The markers △ and ◇ indicate thermal BL thicknesses, and ▲ and ◆ indicate kinetic BL thicknesses for Novec 7200 at 50 Hz and 10 kHz, respectively. Power-law fits of δ_T/d (solid lines) and δ_u/d (dashed lines), combining both loss frequencies, are given in (4.3) and (4.4).

within the fluid layer, we use sequential averaging as discussed in § 4.2. The thermal BL thickness δ_T is defined as the intercept of the linear extrapolation of the near-wall temperature gradient with the bulk fluid temperature T_{bulk}, given by

$$\delta_T = \frac{\delta T}{\left|\partial \langle \overline{T} \rangle_S / \partial z\right|_{wall}}, \tag{4.1}$$

where $\delta T = \langle \overline{T} \rangle_S(z=0) - T_{bulk}$. The kinetic BL thickness follows an equivalent procedure using the velocity magnitude $\langle \overline{U} \rangle_S(z)$. The kinetic BL thickness is defined as the distance from the wall at which the velocity reaches its maximum value in the bulk flow. The slope method defines δ_u as

$$\delta_u = \frac{\overline{U}_{max}}{\left|\partial \langle \overline{U} \rangle_S / \partial z\right|_{wall}}, \tag{4.2}$$

where $\overline{U}_{max}$ is the magnitude of the peak velocity in the bulk of the fluid layer. These definitions provide consistent and reproducible measures of BL thicknesses that relate directly to the local gradients at the boundaries, capturing changes in flow and thermal structure with varying electric forcing. Both of these slope-based definitions are consistent with those employed in Shishkina *et al.* (2010), where the thermal BL thickness is defined through the inverse wall gradient (slope thickness), and the kinetic BL is defined analogously using the velocity gradient.

Figure 4 presents the thermal and kinetic BL thicknesses for both working fluids: figure 4(*a*) for 1-Nonanol, and figure 4(*b*) for Novec 7200. In both cases, the BL thicknesses decrease with increasing electric Rayleigh–Roberts number, indicating enhanced heat transport. Power-law fits yield the following scaling relations:

$$\delta_T \sim 1.27 R_E^{-0.23}, \quad \delta_u \sim 0.143 R_E^{-0.13} \quad \text{(1-Nonanol)}, \tag{4.3}$$

and

$$\delta_T \sim 1.66 R_E^{-0.25}, \quad \delta_u \sim 0.945 R_E^{-0.08} \quad \text{(Novec 7200)}, \tag{4.4}$$

https://doi.org/10.1017/jfm.2026.12105 Published online by Cambridge University Press

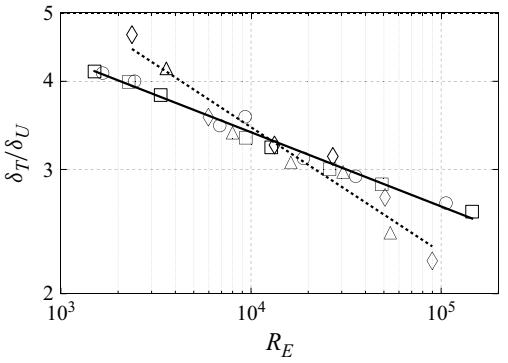


Figure 5. Ratio of the thermal to kinetic BL thicknesses, δ_T/δ_u, versus the electric Rayleigh–Roberts number R_E. The markers ∘ and □ represent 1-Nonanol, and △ and ◊ represent Novec 7200 at 50 Hz and 10 kHz, respectively. Power-law fits of 1-Nonanol (solid line) and Novec 7200 (dashed line) yield $\delta_T/\delta_u \sim R_E^{-0.11}$ and $\delta_T/\delta_u \sim R_E^{-0.18}$, respectively.

where δ_T decreases more rapidly than δ_u in both fluids. The observed thermal BL scaling follows the same decay as reported by Jawichian *et al.* (2021), for dielectric fluid under the influence of the DEP force density, with a slight difference in the scaling exponent ± 0.01. To the best of the authors' knowledge, thermal and kinetic BLs in IH fluids remain unexplored and warrant further investigation.

The observed decay in both power-law slopes (see (4.3) and (4.4)) suggests a possible transition towards the classical BL thicknesses theory of $\delta_T \ll \delta_u$ for larger-Pr fluids. This is also indicated by figure 5, showing the ratio of thermal to kinetic BL thicknesses, δ_T/δ_u, as a function of the electric Rayleigh–Roberts number R_E. The ratio decreases with increasing R_E, following power-law scalings $\delta_T/\delta_u \sim R_E^{-0.11}$ for 1-Nonanol and $\delta_T/\delta_u \sim R_E^{-0.18}$ for Novec 7200. Nonetheless, this comes with limitations due to increased electric forcing, discussed in more detail in § 5. To provide an indication of the dimensional values of the BL thickness in a 1-Nonanol fluid layer of height 5 mm at loss frequency 50 Hz and $V_E = 1900$ ($V_0 = 6430$ kV), the thermal and velocity BL thicknesses are given by $\delta_T = 7.93 \times 10^{-4}$ and $\delta_u = 2.29 \times 10^{-4}$ m, respectively.

The results for the BL indicate that thermal dissipation dominates momentum dissipation within the BL. To elucidate deviations in BL thickness from classical theory, we analyse the time-averaged thermal and kinetic energy dissipation rates, decomposed into bulk and BL contributions. The kinetic energy dissipation is given by

$$\tilde{\varepsilon}_u(\boldsymbol{x}, t) = \tilde{\varepsilon}_u^{BL} + \tilde{\varepsilon}_u^{bulk} = Pr^{-1}\langle(\partial_i \overline{u_j}(\boldsymbol{x} \in \mathrm{BL}))^2\rangle_V + Pr^{-1}\langle(\partial_i \overline{u_j}(\boldsymbol{x} \in \mathrm{bulk}))^2\rangle_V, \quad (4.5)$$

and the thermal energy dissipation reads as

$$\tilde{\varepsilon}_T(\boldsymbol{x}, t) = \tilde{\varepsilon}_T^{BL} + \tilde{\varepsilon}_T^{bulk} = \langle(\partial_i \overline{T}(\boldsymbol{x} \in \mathrm{BL}))^2\rangle_V + \langle(\partial_i \overline{T}(\boldsymbol{x} \in \mathrm{bulk}))^2\rangle_V, \quad (4.6)$$

where $\boldsymbol{x}$ denotes the spatial position vector, and the conditions $\boldsymbol{x} \in$ BL and $\boldsymbol{x} \in$ bulk indicate that the volume averaging is restricted to the BL and bulk regions, respectively. While the bulk thermal dissipation depends on both thermal diffusion and advection (see (2.14)), Grossmann & Lohse (2000) showed that in the regime where $\delta_T > \delta_u$, it can be approximated analogously to kinetic dissipation. This justifies the decomposition in (4.6).

Figure 6 shows the normalised energy dissipation rates in the BL and the bulk regions, defined as $\chi_u^{BL} = \tilde{\varepsilon}_u^{BL}/\tilde{\varepsilon}_u$ and $\chi_u^{bulk} = \tilde{\varepsilon}_u^{bulk}/\tilde{\varepsilon}_u$, respectively. The corresponding ratios for thermal dissipation, denoted with the subscript T, are shown analogously. The results

https://doi.org/10.1017/jfm.2026.12105 Published online by Cambridge University Press

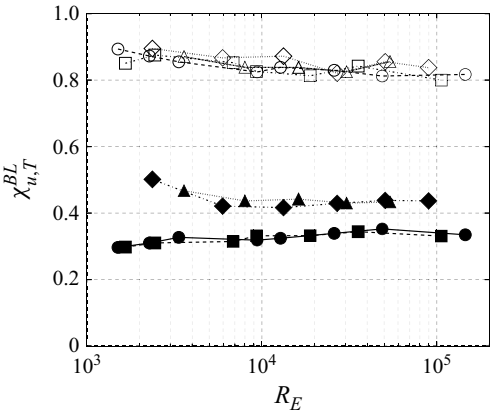


Figure 6. Fraction of energy dissipation rates of the BL fractions of the kinetic energy dissipation rate $\chi_u^{BL} = \tilde{\varepsilon}_u^{BL}/\tilde{\varepsilon}_u$ and thermal dissipation rate $\chi_T^{BL} = \tilde{\varepsilon}_T^{BL}/\tilde{\varepsilon}_T$, plotted as a function of the electric Rayleigh–Roberts number R_E. The corresponding dissipation rate fractions for the bulk region can be evaluated, as the sum of χ_u^{BL} and χ_u^{bulk} equals unity. The markers for 1-Nonanol at 50 Hz and 10 kHz are ○, □ and ●, ■, while △, ◇ and ▲, ◆ denote Novec 7200 at 50 Hz and 10 kHz, respectively. The filled markers represent the kinetic dissipation rate, and the empty markers represent the thermal dissipation rate.

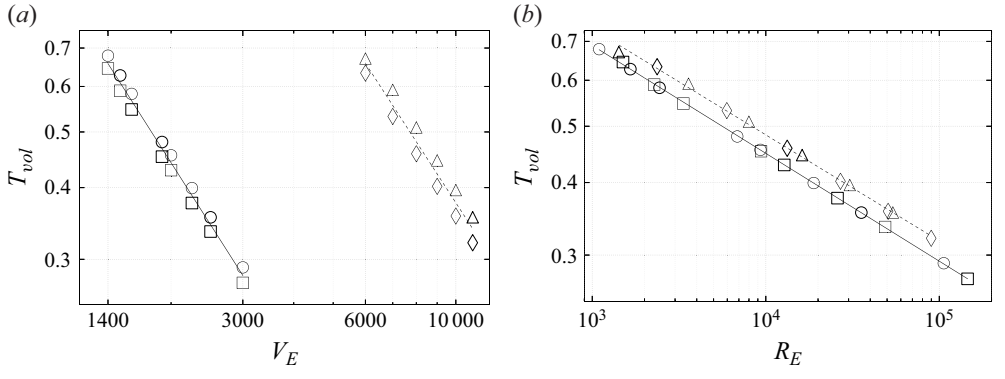


Figure 7. The volume-averaged temperature T_{vol} is plotted as a function of (*a*) the effective voltage V_E, and (*b*) the Rayleigh–Roberts number R_E. The markers ○ and □ represent 1-Nonanol at 50 Hz and 10 kHz, while △ and ◇ denote Novec 7200 at 50 Hz and 10 kHz, respectively. Power-law fits of T_{vol} for 1-Nonanol (solid lines) and for Novec 7200 (dashed lines) are given in (4.7) and (4.8), respectively.

confirm that thermal dissipation is predominantly concentrated within the BLs, rather than the bulk, consistent with the evaluated BL thicknesses.

4.4. *Convective heat transport and scaling*

In the following, we examine the convective heat transport by means of the forcing intensity expressed either by the effective voltage or by the electric Rayleigh–Roberts number. These are given in relation to the volume-averaged temperature, the kinetic energy density and the Nusselt number. The results are compared with established scaling laws in thermal convection, with the main focus on convection in IH fluids.

The volume-averaged temperature T_{vol} within the fluid layer is shown in figures 7(*a,b*) as functions of V_E and R_E, respectively. For both working fluids, T_{vol} decreases with increasing forcing, indicating enhanced advective heat transport in the bulk. Power-law

https://doi.org/10.1017/jfm.2026.12105 Published online by Cambridge University Press

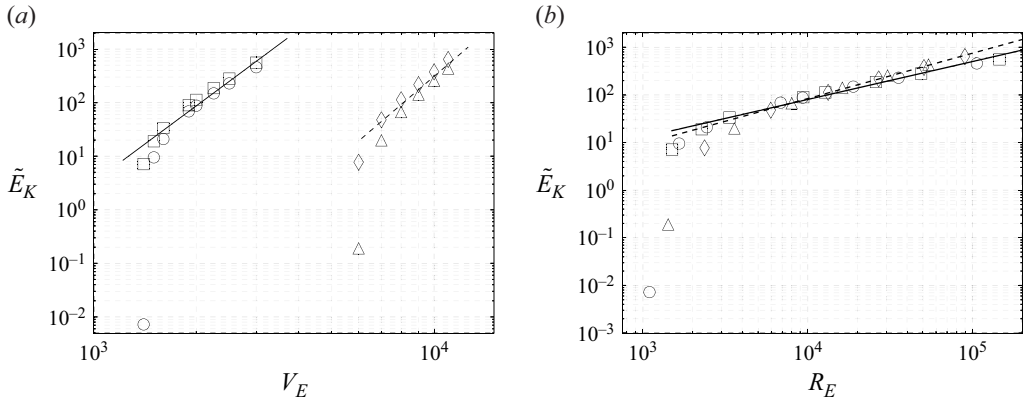


Figure 8. The kinetic energy density $\tilde{E}_K$ is plotted as a function of (*a*) the effective voltage V_E, and (*b*) the Rayleigh–Roberts number R_E. The markers ∘ and □ represent 1-Nonanol at 50 Hz and 10 kHz, while △ and ♢ denote Novec 7200 at 50 Hz and 10 kHz, respectively. Power-law fits of $\tilde{E}_K$ for 1-Nonanol (solid lines) and for Novec 7200 (dashed lines) are given in (4.9) and (4.10), respectively.

fits yield

$$T_{vol} \sim V_E^{-1.11}, \quad T_{vol} \sim 2.49 {R_E}^{-0.19} \quad \text{(1-Nonanol)}, \tag{4.7}$$

and

$$T_{vol} \sim V_E^{-1.09}, \quad T_{vol} \sim 2.6 R_E^{-0.18} \quad \text{(Novec 7200)}, \tag{4.8}$$

with exponents consistent with those reported by Vilella *et al.* (2018), who found $T_{vol} \sim R_E^{-0.192\pm0.033}$ for $R_E \leqslant 5 \times 10^4$, and $T_{vol} \sim R_E^{-0.229\pm0.003}$ for $R_E \geqslant 6.8 \times 10^4$. Similarly, Wang *et al.* (2021) proposed volume-averaged temperature scaling $T_{vol} \sim R_E^{-1/5}$, consistent with the DNS results of Kazemi *et al.* (2022), while a steeper scaling $T_{vol} \sim R_E^{-1/4}$ was predicted for larger Prandtl numbers or turbulent regimes. A comparable $\sim R_E^{-1/4}$ scaling was also reported by Parmentier & Sotin (2000) and further discussed by Vilella *et al.* (2018), who suggested that it provides the best fit across their investigated parameter range. The present trends are in line with $\sim R_E^{-1/4}$ scaling and with the corresponding scaling observed also for the thermal BLs (see (4.3)–(4.4)).

The kinetic energy density $\tilde{E}_K$ quantifies the strength of the convective flow and is presented in figures 8(*a,b*) as functions of V_E and R_E, respectively. As expected, $\tilde{E}_K$ increases with stronger forcing. To relate $\tilde{E}_K$ to transport properties, we define the convective Péclet number as $Pe_c = \sqrt{2\langle \overline{E_K} \rangle}$, representing the ratio of advective to thermal transport. The corresponding convective Reynolds number is given by $Re_c = Pe_c/Pr$, reflecting the balance between advective and viscous effects. Power-law fits yield

$$\tilde{E}_K \sim V_E^{4.71}, \quad \tilde{E}_K \sim R_E^{0.80}, \quad Re_c \sim R_E^{0.40} \quad \text{(1-Nonanol)}, \tag{4.9}$$

and

$$\tilde{E}_K \sim V_E^{5.44}, \quad \tilde{E}_K \sim R_E^{0.95}, \quad Re_c \sim R_E^{0.475} \quad \text{(Novec 7200)}, \tag{4.10}$$

with scaling exponents qualitatively reminiscent of those reported for classical Rayleigh–Bénard convection by Grossmann & Lohse (2000). However, the present range of R_E does not reach the regime in which the Grossmann–Lohse theory is expected to be strictly applicable. Therefore, the comparison should be understood only as a qualitative analogy

https://doi.org/10.1017/jfm.2026.12105 Published online by Cambridge University Press

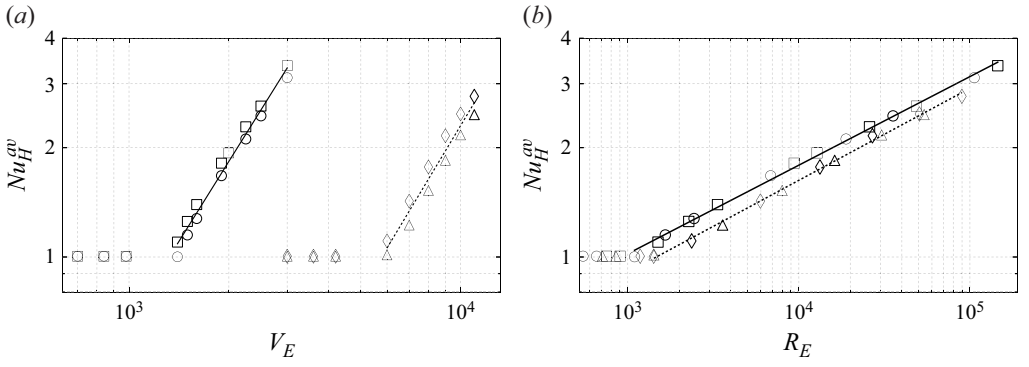


Figure 9. The average Nusselt number Nu_H^{av} plotted as a function of (*a*) the effective voltage V_E, and (*b*) the electric Rayleigh–Roberts number R_E. The markers ∘ and □ represent 1-Nonanol at 50 Hz and 10 kHz, while △ and ♢ denote Novec 7200 at 50 Hz and 10 kHz, respectively. Power-law fits of Nu_H^{av} for 1-Nonanol (solid lines) and for Novec 7200 (dashed lines) are given in (4.11) and (4.12), respectively.

rather than a direct validation of the predicted Reynolds number scaling exponent of approximately 0.5 for regime I_u at moderate Rayleigh numbers and moderate Pr.

The Nusselt number Nu_H (see (C1)) characterises the heat transfer intensity and allows correlation with the forcing parameters. In the Kulacki & Goldstein (1972) laboratory experiments, Nu_H was computed separately at the upper and lower boundaries due to asymmetries in heat dissipation. In contrast, under microgravity conditions considered in the present numerical study, no significant difference was observed in Nu_H between the two boundaries, indicating symmetric thermal behaviour in the absence of Archimedean buoyancy-driven natural convection. Thermal equilibrium is considered established when the relative difference between the heat fluxes at the bounding plates falls below $\pm 2\,\%$. At this point, a time-averaged Nusselt number Nu_H^{av} can be evaluated, characterising the mean heat transfer across both boundaries in the IH system. The results for Nu_H^{av} are plotted in figures 9(*a,b*) as functions of V_E and R_E, respectively. Power-law fits yield the scalings

$$Nu_H^{av} \sim V_E^{1.463\pm0.050}, \quad Nu_H^{av} \sim 0.189 R_E^{0.244\pm0.004} \quad \text{(1-Nonanol)}, \tag{4.11}$$

and

$$Nu_H^{av} \sim V_E^{1.518\pm0.105}, \quad Nu_H^{av} \sim 0.158 R_E^{0.253\pm0.004} \quad \text{(Novec 7200)}, \tag{4.12}$$

which is consistent with the scaling exponent of R ranging from 0.219 to 0.360, reported by Goluskin (2016) in their table 3.2.

Figure 9(*b*) highlights a clear difference in the onset of convection between the two working fluids. This behaviour is consistent with the findings of Yoshikawa *et al.* (2020), who showed through a linear stability analysis that variations in the thermoelectric parameter γ_e shift the critical onset of convection. Our results support this trend, demonstrating that the critical electric Rayleigh–Roberts number R_E^{crit} increases as γ_e decreases. Since Novec 7200 exhibits a significantly lower γ_e than 1-Nonanol, convection in Novec 7200 initiates at a higher R_E, while 1-Nonanol exhibits an earlier onset.

5. Discussion and limitations

This section compares the present study on internal dielectric heating in fluid layers with previous investigations of IH systems, as well as classical boundary-driven configurations such as Rayleigh–Bénard and TEHD convection.

https://doi.org/10.1017/jfm.2026.12105 Published online by Cambridge University Press

The present study extends the experimental work of Kulacki & Goldstein (1972) and the numerical investigations by Vilella *et al.* (2018) by incorporating internal dielectric heating and thermoelectric coupling, guided by the theoretical framework and linear stability analysis of Yoshikawa *et al.* (2020). Comparable scaling laws for IH flows remain limited in the literature. Nevertheless, the observed scaling exponents for thermal BL and T_{vol} agree with previous studies (see Kulacki & Goldstein 1972; Parmentier & Sotin 2000; Moore 2008; Vilella *et al.* 2018; Wang *et al.* 2021; Kazemi *et al.* 2022).

Notably, we observe $\delta_T \gg \delta_u$ for fluids of large Prandtl numbers, where $\delta_T \ll \delta_u$ is generally expected in classical boundary-heated systems causing natural convection. However, the explored parameter range, with R_E up to 10^5, remains relatively limited. The notion of a BL implies that its thickness must be much smaller than the characteristic size of the domain. In this regime, the comparatively large thermal diffusivity leads to a thermal BL that is thicker than the velocity BL. This behaviour is consistent e.g. with classical Rayleigh–Bénard convection. The present scaling exponents should therefore be interpreted as indicators of the dominant transport mechanisms over the limited investigated range of R_E up to 10^5 rather than as asymptotic laws analogous to larger forcing like Kulacki & Goldstein (1972), Vilella *et al.* (2018) or Rayleigh–Bénard convection. Different power laws emerge depending on whether kinetic and thermal dissipation are dominated by the BLs or by the bulk. The corresponding scaling exponents therefore reflect changes in the dominant energy and heat transport balances rather than universal constants. Although the thermal BL thins substantially with increasing forcing, the kinetic BL remains comparatively thick over the accessible parameter range, indicating that the momentum field has not yet reached an asymptotic scaling regime. The observed differences in the exponential decay of the BL ratio indicate a dependence on the Prandtl number, and suggest a transition towards BL thicknesses where $\delta_T \ll \delta_u$, a behaviour characteristic of fluids with higher Pr and larger R_E, but accompanied by constraints discussed in more detail below related to the electric breakdown voltage (see Szabo & Egbers 2025). Although the influence of the forcing parameter γ_e is not addressed here for larger values, its potential impact warrants further investigation.

To study BL thicknesses for larger values in R_E for the expected intercept of power laws as discussed above may not be feasible, as it is in contrast to the dielectric breakdown voltage. For typical commercially available dielectric fluids, electric Rayleigh numbers for boundary-heated fluid layers range from 10^4 to 10^5 and are currently achievable in laboratory environments (see Barry *et al.* 2023; Kang *et al.* 2024; Szabo & Egbers 2025). The dielectric breakdown voltage of these fluids depends on their polarity and insulating behaviour. Polar fluids, such as hydrofluoroethers (e.g. Novec 7200), exhibit slightly lower breakdown voltages approximately $23.8\,\mathrm{kV\,mm^{-1}}$. Although these fluids are still effective insulators, their inherent polarity contributes to a modest decrease in dielectric strength. Strongly polar fluids, such as 1-Nonanol (an alcohol-based liquid), demonstrate even lower breakdown thresholds, approximately $20.7\,\mathrm{kV\,mm^{-1}}$, due to their increased conductivity and interaction with electric fields. A range of factors can affect the breakdown performance of dielectric fluids, including the presence of moisture, contaminants, electrode configuration and experimental set-up. Overall, non-polar fluids are typically favoured for high-voltage uses due to their superior insulation properties. To enhance the electric Rayleigh–Roberts number, various frequency ranges of the applied alternating electric voltage can be examined in order to identify the maximum loss factor, thereby extending the feasible range of the forcing parameter.

The convective Reynolds number scales as $Re_c \sim R_E^{0.400-0.475}$, which is qualitatively similar to the $Re_c \sim Ra^{0.5}$ dependence predicted by the Grossmann & Lohse (2000) theory

https://doi.org/10.1017/jfm.2026.12105 Published online by Cambridge University Press

for Rayleigh–Bénard convection, although the accessible forcing range remains well below the asymptotic regime where that theory is expected to apply. This similarity suggests that the increase in kinetic energy is primarily associated with the strengthening of the large-scale circulation for relative small R_E rather than with a transition to turbulence.

The thermal BL scaling, the reduction of the volume-averaged temperature, the increase in the convective Reynolds number and the increase in the Nusselt number are mutually consistent. As R_E increases, stronger convective motion enhances advective transport within the bulk, reducing T_{vol} while simultaneously thinning the thermal BL. Since the conductive resistance of the BL decreases with decreasing δ_T, the resulting increase in heat transfer naturally produces the observed Nu_H^{av} scaling. In particular, the resulting scaling exponent aligns remarkably well with previous laboratory studies of IH fluids conducted under gravity conditions, and is comparable in magnitude to the classical Rayleigh–Bénard scaling exponent 0.25 (see Kulacki & Goldstein 1972; Grossmann & Lohse 2000).

However, no significant variation in the scaling exponents is observed with respect to Pr in the range of explored parameters. This suggests that within the investigated parameter range, the DEP force density primarily governs the large-scale circulation, while molecular diffusivities mainly influence the prefactors rather than the scaling exponents. Whether this behaviour persists at larger R_E or reflects the limited range of accessible forcing remains an open question.

One has to note that for boundary-heated fluid layers, Jawichian *et al.* (2021) observed no significant dependence of Pr on Nu_B at large electric Rayleigh numbers denoted in their study by variable L. This finding contrasts with classical natural convection, where Nu_B typically scales with both Ra and Pr. For example, Tritton (1977) provides $Nu_B = f(Ra, Pr)$, while Grossmann & Lohse (2000) reported a scaling $Nu_B \sim Ra^{1/4}\, Pr^{-1/12}$ for $Pr \gtrsim 1$. This raises questions about the governing diffusion mechanisms in TEHD convection, both in the bulk and within the BLs. However, previous studies have reported a dependence on Pr away from the onset of TEHD convection. The classical numerical study of the onset of TEHD convection by Yoshikawa *et al.* (2013*b*) (see their figure 7) also indicated a Pr dependence at larger electric Rayleigh numbers, but the trend is not clearly given. Szabo & Egbers (2025) have shown a Pr dependence using an electrode configuration similar to that reported in Jawichian *et al.* (2020); a similar observation was made by Travnikov *et al.* (2015) in cylindrical annuli. In the latter, the influence of Pr on Nu_B varied in addition with the radius ratio η, with more pronounced effects at smaller η, particularly closer to the onset of convection. Notably, all studies incorporate thermoelectric feedback via the parameter γ_e in the electrostatic Gauss equation, which is known to influence the onset and heat transfer in TEHD convection demonstrated in planar layers (see Yoshikawa *et al.* 2013*b*), cylindrical geometries (see Travnikov *et al.* 2015, 2016) and dielectrically heated fluids (see Yoshikawa *et al.* 2020).

6. Conclusion

The behaviour of two distinct Prandtl number fluids subjected to dielectric heating in a confined fluid layer, cooled from opposite bounding plates, was explored through 3-D numerical simulations under microgravity conditions. The resulting convective structures were categorised based on their temporal and topological behaviour into four groups as the electric Rayleigh–Roberts number increased: stable hexagonal patterns, mixed hexagonal-square structures, dominant rectangular patterns and time-dependent convection. The spatial distribution of temperature and velocity, averaged over cross-sections, displayed the structural differences between the groups.

https://doi.org/10.1017/jfm.2026.12105 Published online by Cambridge University Press

Scaling laws were formulated for key dimensionless quantities, including volume-averaged temperature and kinetic energy density, the convective Reynolds number and the Nusselt number, correlating with simulation results across a two-orders-of-magnitude range in the electric Rayleigh–Roberts number. The variation in the onset of convection was associated with the thermoelectric parameter, showing a shift in the critical threshold. Our findings confirm this trend, that the critical electric Rayleigh–Roberts number increases as the thermoelectric parameter decreases.

Acknowledgements. The authors want to thank A. Meyer, O. Crumeyrolle, I. Mutabazi and U. Harlander for fruitful discussions about convection in dielectric heated fluid layers, and V. Motuz and M. Hamede, who are pursuing the experimental realisation of the present study.

Funding. This work was supported by four research projects. The projects 'AtmoFlow' (grant nos 50WP2209, 50WM1841, 50WM2141 and 50WM2441), 'TEKUS' and its successor 'DEPIC' (grant nos 50WP1644, 50WM1944 and 50WM2244) and 'AID2' (grant no. 50WM2354) were funded by the German Federal Ministry for Economic Affairs and Climate Action (BMWK) through the German Aerospace Centre (DLR). The authors further acknowledge support from the German Federal Ministry of Education and Research, and the German federal states as part of the National High-Performance Computing (NHR) joint funding programme under grant no. bbi00021 (http://www.nhr-verein.de/en/our-partners).

Declaration of interests. The authors report no conflict of interest.

Author contributions. P.S.B.S.: conceptualisation, methodology, validation, formal analysis, investigation, resources, data creation, writing original and final draft, review and editing, visualisation, project administration, funding acquisition. K.N.: methodology, conceptualisation, investigation, numerical simulations, formal analysis, data creation, visualisation, validation, review and editing, preparation of draft. Y.A.M.: numerical simulations, data creation, preparation of draft. M.S.: preparation of draft. C.E.: project administration, funding acquisition. F.Z.: review and editing, visualisation. All authors have read and agreed to the published version of the paper.

Appendix A. Fluid properties

The physical properties of the two working fluids used in this study, Novec 7200 and 1-Nonanol, are summarised in table 2. These include the thermophysical and dielectric properties evaluated at the reference temperature T_0, listed along with the characteristic time scales and the resulting Prandtl numbers.

Appendix B. Numerical implementation and discretisation

The simulations are performed using a finite-volume technique within OpenFOAM v2012, employing a custom-modified `buoyantPimpleFoam` solver (Gaillard *et al.* 2024, 2025). The numerical procedure consists of two stages. In the first stage, the energy equation (2.14) and Gauss's law (2.15) are solved to obtain the initial electrostatic and thermal fields. The resulting electric field gradient is subsequently used to initialise the fully coupled, transient computation of the velocity, pressure, temperature and electric potential fields.

Spatial discretisation follows established second-order-accurate schemes. Divergence terms are approximated using the `Gauss linear` scheme, while Laplacian terms are treated with the `Gauss linear corrected` formulation to ensure accuracy on non-orthogonal meshes. Surface-normal gradients are evaluated using the `corrected` option within `snGradSchemes`, reducing numerical diffusion. Field interpolation is performed using the `linear` scheme, and gradients are computed via the `leastSquares` method for robustness on irregular meshes. Temporal integration is carried out using a second-order `Crank-Nicolson` scheme with blending factor 0.9, providing a balance between stability and temporal accuracy in transient simulations.

https://doi.org/10.1017/jfm.2026.12105 Published online by Cambridge University Press

The pressure equation is solved using the geometric–algebraic multi-grid (`GAMG`) solver. The momentum and energy equations are handled using the preconditioned bi-conjugate gradient stabilised (`PBiCGStab`) solver with a diagonal incomplete LU (`DILU`) preconditioner, which is well suited for non-symmetric systems. The electric potential equation is solved separately using `GAMG` with diagonal incomplete Cholesky (`DIC`) smoothing and forward DIC (`FDIC`) preconditioning.

The coupling between pressure and velocity is achieved via the pressure-implicit with splitting of operators (`PIMPLE`) algorithm. The electric field and corresponding DEP force density are updated at each outer PIMPLE iteration. Multiple non-orthogonal correction steps and residual controls are employed to ensure numerical stability and convergence. All simulations are parallelised using OpenMPI, as implemented natively in OpenFOAM.

Appendix C. Benchmark validation and mesh-independence study

Prior to the present investigation, the numerical solver was validated for natural convection and TEHD convection in a series of benchmark studies (Gaillard *et al.* 2024, 2025), demonstrating deviations of less than 1 % when compared with pseudo-spectral and finite-element solutions.

To further validate the numerical approach for a non-isothermal fluid layer, we perform additional benchmark simulations using the configuration of Barry *et al.* (2023). The boundary conditions follow equations (3*a*)–(3*d*) and (7*a*)–(7*b*) of that study. We consider a commercial silicone oil with Prandtl number $Pr = 65$ and electric permittivity $\gamma_e = 0.03$. The heat transfer is quantified by the Nusselt number

$$Nu_B = \frac{\dot{q}_t}{\dot{q}_c}, \tag{C1}$$

where $\dot{q}_t$ denotes the total heat flux, and $\dot{q}_c$ denotes the conductive heat flux across the differentially heated, adiabatic boundaries. For the benchmark case discussed in § 3.4, $\dot{q}_c$ is given analytically by $\dot{q}_c = k\Delta T/d$, while $\dot{q}_t$ is obtained numerically. In boundary-heated fluid layers, $Nu_B = 1$ corresponds to purely conductive transport, whereas $Nu_B > 1$ indicates convective enhancement. Figure 10(*a*) shows Nu_B for equilibrated flow states as a function of the electric Rayleigh number

$$L = \frac{\alpha\ \Delta T\ g_e d^3}{\nu\kappa}, \tag{C2}$$

where g_e is the electric gravity evaluated at the reference position defined in equation (4) of Barry *et al.* (2023). The results exhibit excellent agreement with the reference data over the entire parameter range, with deviations remaining below 1 % even at the highest Rayleigh numbers.

The computational domain shown in figure 1 is discretised using OpenFOAM's built-in `blockMesh` generator. Uniform cell spacing is employed in the bounding plate direction, while boundary-layer refinement in the wall-normal direction is achieved using a simple grading scheme with refinement ratio 0.1. This ensures adequate resolution of near-wall gradients while maintaining computational efficiency.

Mesh-convergence is achieved for meshes with at least **xCells** = 200, **yCells** = 200 and **zCells** = 40, corresponding to approximately 3.2×10^4 cells for the 2-D geometry, and 1.6×10^6 cells for the 3-D geometry. Mesh-independence tests indicate deviations of less than 2 % in key global quantities, such as the kinetic and thermal energy densities, as illustrated in figure 10(*b*).

https://doi.org/10.1017/jfm.2026.12105 Published online by Cambridge University Press

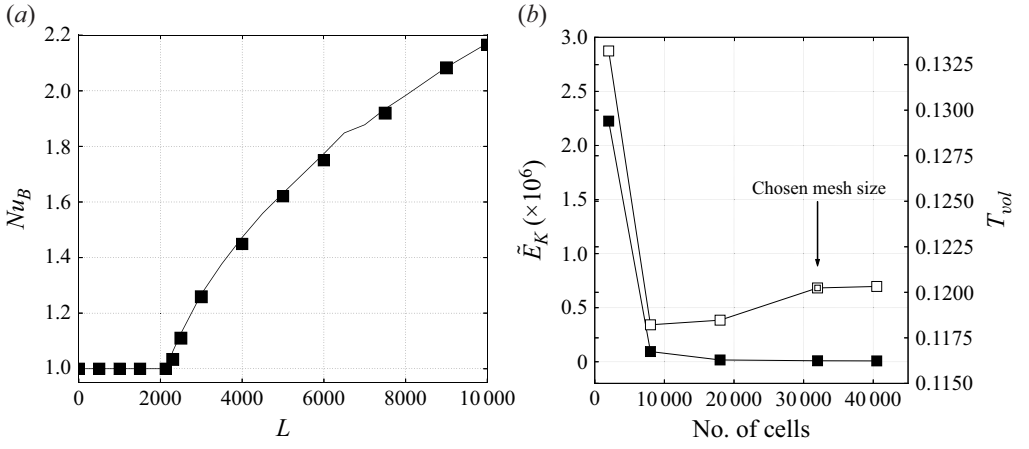


Figure 10. (*a*) The Nusselt number Nu_B for equilibrated flow states as a function of the boundary heated electric Rayleigh number L at $Pr = 65$ and $\gamma_e = 0.03$. This is shown for comparison with figure 5 in Barry *et al.* (2023) (■ denote simulation data; black line for Barry *et al.* (2023), where the definition of L is found). (*b*) Mesh independence study: kinetic energy density $\tilde{E}_K$ (■) and volume-averaged temperature T_{vol} (□), plotted as functions of the total number of cells at $R_E = 7 \times 10^6$.

Appendix D. The BL thickness

The thermal and kinetic BL thicknesses are denoted by δ_T and δ_u, and calculated using a linear approximation by using the slope method introduced by Shishkina *et al.* (2010). Before calculating the BL thickness, the 3-D fields are first temporal averaged and then spatial averaged via sections first in the $y-z$ plane and then in the $x-z$ plane, denoted by $\langle\cdot\rangle_S$ to evaluate the wall near fields. For the thermal BL thickness, a first-order Taylor expansion gives

$$\langle\overline{T}\rangle_S(z) \approx \langle\overline{T}\rangle_S(z=0) + \left.\frac{\partial\langle\overline{T}\rangle_S}{\partial z}\right|_{wall}, \tag{D1}$$

and at $z = \delta_t$, $\langle\overline{T}\rangle_S(z)$ becomes

$$\overline{T}_{bulk} \approx \langle\overline{T}\rangle_S(z=0) + \left.\frac{\partial\langle\overline{T}\rangle_S}{\partial z}\right|_{wall}\delta_t. \tag{D2}$$

By rearranging, we obtain

$$\delta_T = \frac{\overline{T}_{bulk} - \langle\overline{T}\rangle_S(z=0)}{\left|\partial\overline{T}/\partial z\right|_{wall}} \quad \Rightarrow \quad \delta_T = \frac{\delta T}{\left|\partial\overline{T}/\partial z\right|_{wall}}, \tag{D3}$$

which is the thermal BL thicknesses. Similarly, the kinetic BL thickness is where the flow reaches the maximum of the velocity magnitude, $\overline{U}_{max}$:

$$\langle\overline{U}\rangle_S(z) \approx \langle\overline{U}\rangle_S(z=0) + \left.\frac{\partial\langle\overline{U}\rangle_S}{\partial z}\right|_{wall} z. \tag{D4}$$

For the no-slip boundary condition $\overline{U}(z = [0, 1]) = 0$,

$$\langle\overline{U}\rangle_S(z) \approx \left.\frac{\partial\langle\overline{U}\rangle_S}{\partial z}\right|_{wall} z, \tag{D5}$$

https://doi.org/10.1017/jfm.2026.12105 Published online by Cambridge University Press

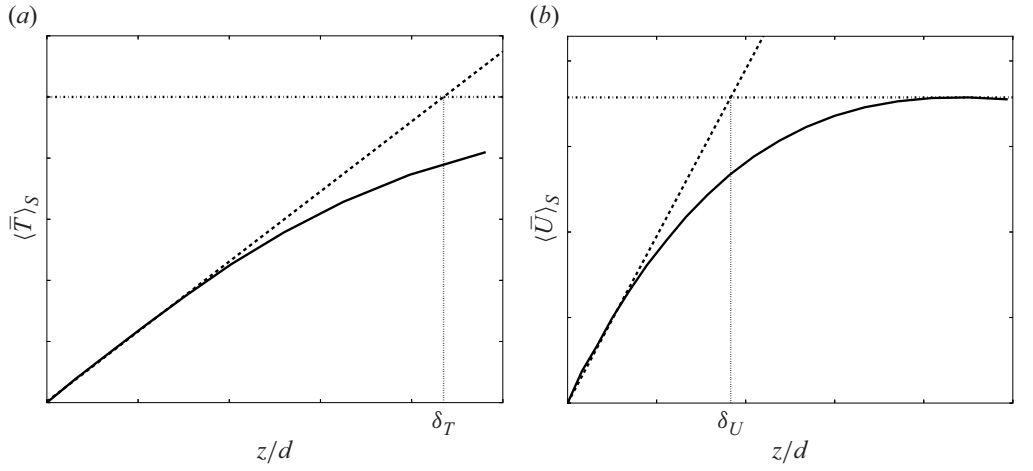


Figure 11. Schematics of the slope-fitting procedure for determining the (*a*) thermal and (*b*) kinetic BL thicknesses. The time- and section-averaged profiles are shown by solid lines, the linear fits by dashed lines, the BL thicknesses by dotted lines, and the bulk profiles by dash-dotted lines, according to Shishkina *et al.* (2010).

and we obtain

$$\overline{U}_{max} \approx \left.\frac{\partial\langle\overline{U}\rangle_S}{\partial z}\right|_{wall} \delta_u \quad \Rightarrow \quad \delta_u = \frac{\overline{U}_{max}}{\left|\partial\langle\overline{U}\rangle_S/\partial z\right|_{wall}}, \tag{D6}$$

which is the thicknesses of the kinetic BL. Both of these slope-based definitions are consistent with those employed in Shishkina *et al.* (2010), where the thermal BL thickness is defined via the inverse wall gradient (slope thickness), and the kinetic BL thickness is defined analogously using the velocity gradient.

References

Arslan, A. 2024 Internally heated convection with rotation: bounds on heat transport. *J. Fluid Mech.* **1001**, A55.

Arslan, A., Fantuzzi, G., Craske, J. & Wynn, A. 2021*a* Bounds for internally heated convection with fixed boundary heat flux. *J. Fluid Mech.* **922**, R1.

Arslan, A., Fantuzzi, G., Craske, J. & Wynn, A. 2021*b* Bounds on heat transport for convection driven by internal heating. *J. Fluid Mech.* **919**, A15.

Arslan, A., Fantuzzi, G., Craske, J. & Wynn, A. 2023 Rigorous scaling laws for internally heated convection at infinite Prandtl number. *J. Math. Phys.* **64** (2), 023101.

Arslan, A. & Rojas, R.E. 2025 New bounds for heat transport in internally heated convection at infinite Prandtl number. *J. Math. Phys.* **66** (2), 023101.

Barry, E.B., Kang, C., Yoshikawa, H.N. & Mutabazi, I. 2023 Flow patterns and heat transfer in a dielectric liquid inside a planar capacitor under microgravity conditions. *Appl. Phys. Lett.* **122** (18), 182903.

Beltrame, P., Egbers, C. & Hollerbach, R. 2003 The GEOFLOW-experiment on ISS (part III): bifurcation analysis. *Adv. Space Res.* **32** (2), 191–197.

Boussinesq, J. 1903 *Théorie Analytique de la Chaleur: Mise en Harmonie avec la Thermodynamique et avec la Théorie Mécanique de la Lumière*, vol. 2. Gauthier-Villars.

Chandra, B. & Smylie, D.E. 1972 A laboratory model of thermal convection under a central force field. *Geophys. Fluid Dyn.* **3** (3), 211–224.

Egbers, C., Beyer, W., Bonhage, A., Hollerbach, R. & Beltrame, P. 2003 The geoflow-experiment on ISS (part I): experimental preparation and design of laboratory testing hardware. *Adv. Space Res.* **32** (2), 171–180.

Emara, A.A. & Kulacki, F.A. 1980 A numerical investigation of thermal convection in a heat-generating fluid layer. *J. Heat Mass Transfer* **102** (3), 531–537.

https://doi.org/10.1017/jfm.2026.12105 Published online by Cambridge University Press

FIEDLER, H.E. & WILLE, R. 1970 Turbulente freie konvektion tn einer horizontalen flussigkeitsschicht mit volumen-warmequelle. In *International Heat Transfer Conference Digital Library*. Begel House Inc.

FUTTERER, B., EGBERS, C., DAHLEY, N., KOCH, S. & JEHRING, L. 2010 First identification of sub- and supercritical convection patterns from 'GeoFlow', the geophysical flow simulation experiment integrated in fluid science laboratory. *Acta Astronaut.* **66** (1–2), 193–200.

FUTTERER, B., KREBS, A., PLESA, A.-C., ZAUSSINGER, F., HOLLERBACH, R., BREUER, D. & EGBERS, C. 2013 Sheet-like and plume-like thermal flow in a spherical convection experiment performed under microgravity. *J. Fluid Mech.* **735**, 647–683.

GAILLARD, Y., SZABO, P.S.B. & EGBERS, C. 2026 Convection in spherical Taylor–Couette flow under the influence of the dielectrophoretic force. *J. Fluid Mech.* **1033**, A4.

GAILLARD, Y., SZABO, P.S.B., TRAVNIKOV, V. & EGBERS, C. 2024 Thermo-electrohydrodynamic convection in a rotating shell with central force field. *Intl J. Heat Mass Transfer* **218**, 124760.

GAILLARD, Y., SZABO, P.S.B., TRAVNIKOV, V. & EGBERS, C. 2025 Modelling thermo-electrohydrodynamic convection in rotating spherical shell using OpenFOAM®. *OpenFOAM® J.* **5**, 1–16.

GOLUSKIN, D. 2016 *Internally Heated Convection and Rayleigh–Bénard Convection*. Springer.

GOLUSKIN, D. & VAN DER POEL, E.P. 2016 Penetrative internally heated convection in two and three dimensions. *J. Fluid Mech.* **791**, R6.

GOLUSKIN, D. & SPIEGEL, E.A. 2012 Convection driven by internal heating. *Phys. Lett. A* **377** (1–2), 83–92.

GROSSMANN, S. & LOHSE, D. 2000 Scaling in thermal convection: a unifying theory. *J. Fluid Mech.* **407**, 27–56.

HART, J.E., GLATZMAIER, G.A. & TOOMRE, J. 1986 Space-laboratory and numerical simulations of thermal convection in a rotating hemispherical shell with radial gravity. *J. Fluid Mech.* **173**, 519–544.

JAWICHIAN, A., DAVOUST, L. & SIEDEL, S. 2020 Heat transfer enhancement by a non-uniform electric field in microgravity conditions. *Phys. Fluids* **32** (6), 067113.

JAWICHIAN, A., DAVOUST, L. & SIEDEL, S. 2021 Dielectrophoresis-driven jet impingement heat transfers in microgravity conditions. *Phys. Fluids* **33** (7), 073609.

JONES, T.B. 1979 Electrohydrodynamically enhanced heat transfer in liquids – a review. *Adv. Heat Transfer* **14**, 107–148.

KANG, C., MUTABAZI, I. & YOSHIKAWA, H.N. 2024 Thermoelectrohydrodynamic convection in a finite cylindrical annulus under microgravity. *J. Fluid Mech.* **991**, A7.

KAZEMI, S., OSTILLA-MÓNICO, R. & GOLUSKIN, D. 2022 Transition between boundary-limited scaling and mixing-length scaling of turbulent transport in internally heated convection. *Phys. Rev. Lett.* **129** (2), 024501.

KULACKI, F.A. & EMARA, A.A. 1977 Steady and transient thermal convection in a fluid layer with uniform volumetric energy sources. *J. Fluid Mech.* **83** (2), 375–395.

KULACKI, F.A. & GOLDSTEIN, R.J. 1972 Thermal convection in a horizontal fluid layer with uniform volumetric energy sources. *J. Fluid Mech.* **55** (2), 271–287.

KULACKI, F.A. & NAGLE, M.E. 1975 Natural convection in a horizontal fluid layer with volumetric energy sources. *J. Heat Mass Transfer* **97** (2), 204–211.

KUMAR, A., ARSLAN, A., FANTUZZI, G., CRASKE, J. & WYNN, A. 2022 Analytical bounds on the heat transport in internally heated convection. *J. Fluid Mech.* **938**, A26.

LANDAU, L.D., LIFSHITS, E.M. & PITAEVSKIĬ, L.P. 1984 *Electrodynamics of Continuous Media*. Pergamon Press Ltd.

LEE, S.D., LEE, J.K. & SUH, K.Y. 2007 Boundary condition dependent natural convection in a rectangular pool with internal heat sources. *J. Heat Transfer* **129** (5), 679–682.

MCKENZIE, D., ROBERTS, J. & WEISS, N. 1973 Numerical models of convection in the Earth's mantle. *Tectonophysics* **19** (2), 89–103.

MEIER, M., JONGMANNS, M., MEYER, A., SEELIG, T., EGBERS, C. & MUTABAZI, I. 2018 Flow pattern and heat transfer in a cylindrical annulus under 1 g and low-g conditions: experiments. *Microgravity Sci. Technol.* **30**, 699–712.

MOORE, W.B. 2008 Heat transport in a convecting layer heated from within and below. *J. Geophys. Res.: Solid Earth* **113** (B11), B11407.

MUTABAZI, I., YOSHIKAWA, H.N., FOGAING, M.T., TRAVNIKOV, V., CRUMEYROLLE, O., FUTTERER, B. & EGBERS, C. 2016 Thermo-electro-hydrodynamic convection under microgravity: a review. *Fluid Dyn. Res.* **48** (6), 061413.

NAKAGAWA, T. & TACKLEY, P.J. 2014 Influence of combined primordial layering and recycled MORB on the coupled thermal evolution of Earth's mantle and core. *Geochem. Geophys. Geosyst.* **15** (3), 619–633.

https://doi.org/10.1017/jfm.2026.12105 Published online by Cambridge University Press

OSTILLA-MÓNICO, R. & ARSLAN, A. 2025 Rotationally affected internally heated convection. *J. Fluid Mech.* **1018**, A31.

PARMENTIER, E.M. & SOTIN, C. 2000 Three-dimensional numerical experiments on thermal convection in a very viscous fluid: implications for the dynamics of a thermal boundary layer at high Rayleigh number. *Phys. Fluids* **12** (3), 609–617.

PECKOVER, R.S. & HUTCHINSON, I.H. 1974 Convective rolls driven by internal heat sources. *Phys. Fluids* **17** (7), 1369–1371.

RICARD, Y. 2007 Physics of mantle convection. *Treatise Geophys.* **7**, 31–87.

ROBERTS, P.H. 1967 Convection in horizontal layers with internal heat generation. Theory. *J. Fluid Mech.* **30** (1), 33–49.

ROBERTS, P.H. 1969 Electrohydrodynamic convection. *Q. J. Mech. Appl. Maths* **22** (2), 211–220.

SAMUEL, H. & FARNETANI, C.G. 2003 Thermochemical convection and helium concentrations in mantle plumes. *Earth Planet. Sci. Lett.* **207** (1–4), 39–56.

SCHUBERT, G., TURCOTTE, D. & OLSON, P. 2001 *Mantle Convection in the Earth and Planets*. Cambridge University Press.

SENFTLEBEN, H. 1932 Über den einfluß von magnetischen und elektrischen feldern auf den wärmestrom in gasen. *Z. Phys.* **74** (11–12), 757–769.

SENFTLEBEN, H. & BRAUN, W. 1936 Der einfluss elektrischer felder auf den wärmestrom in gasen. *Z. Phys.* **102** (7–8), 480–506.

SENFTLEBEN, H. & PIETZNER, J. 1933 Die einwirkung magnetischer felder auf das wärmeleitvermögen von gasen. I. *Ann. Phys. Berlin* **408** (8), 907–929.

SHISHKINA, O., STEVENS, R.J.A.M., GROSSMANN, S. & LOHSE, D. 2010 Boundary layer structure in turbulent thermal convection and its consequences for the required numerical resolution. *New J. Phys.* **12** (7), 075022.

SMORODIN, B.L. & VELARDE, M.G. 2001 On the parametric excitation of electrothermal instability in a dielectric liquid layer using an alternating electric field. *J. Electrostat.* **50** (3), 205–226.

STILES, P.J. 1991 Electro-thermal convection in dielectric liquids. *Chem. Phys. Lett.* **179** (3), 311–315.

STRANGFELD, M., BÖLÜK, O., SZABO, P., MEIER, M., MEYER, A., SLIAVIN, Y., MOTUZ, V. & EGBERS, C. 2022 Thermo-electrohydrodynamic convection in a dielectric fluid layer with volumetric heating. In *GALA-Fachtagung 'Experimentelle Strömungsmechanik'*, pp. 43.1–43.8. GALA.

STRAUS, J.M. 1976 Penetrative convection in a layer of fluid heated from within. *Astrophys. J.* **209**, 179–189.

SZABO, P.S.B. & EGBERS, C. 2025 Dielectrophoretic-driven thermoelectrohydrodynamic convection in a dielectric fluid layer induced by an inhomogeneous external electric field. *Phys. Rev. E* **111** (4), 045105.

SZABO, P.S.B., GAILLARD, Y., ZAUSSINGER, F. & EGBERS, C. 2023 Thermo-electrohydrodynamic convection in a differentially heated shell with electric central force field. *Proc. Appl. Maths Mech.* **23** (1), e202200121.

SZABO, P.S.B., MEIER, M., MEYER, A., BARRY, E., MOTUZ, V., MUTABAZI, I. & EGBERS, C. 2021 PIV and shadowgraph measurements of thermo-electrohydrodynamic convection in a horizontal aligned differentially heated annulus at different gravity conditions. *Exp. Therm. Fluid Sci.* **129**, 110470.

SZABO, P.S.B., MEYER, A., MEIER, M., MOTUZ, V., SLIAVIN, Y. & EGBERS, C. 2022 Simultaneous PIV and shadowgraph measurements of thermo-electrohydrodynamic convection in a differentially heated annulus. *Technisches Messen* **89** (3), 148–157.

TAKASHIMA, M. 1976 The effect of rotation on electrohydrodynamic instability. *Can. J. Phys.* **54** (3), 342–347.

TAKASHIMA, M. 1980 Electrohydrodynamic instability in a dielectric fluid between two coaxial cylinders. *Q. J. Mech. Appl. Maths* **33** (1), 93–103.

TRAVNIKOV, V., CRUMEYROLLE, O. & MUTABAZI, I. 2015 Numerical investigation of the heat transfer in cylindrical annulus with a dielectric fluid under microgravity. *Phys. Fluids* **27** (5), 054103.

TRAVNIKOV, V., CRUMEYROLLE, O. & MUTABAZI, I. 2016 Influence of the thermo-electric coupling on the heat transfer in cylindrical annulus with a dielectric fluid under microgravity. *Acta Astronaut.* **129**, 88–94.

TRAVNIKOV, V. & EGBERS, C. 2021 Numerical investigation of atmospherelike flows in a spherical geometry. *Phys. Rev. E* **104** (6), 065110.

TRAVNIKOV, V., EGBERS, C. & HOLLERBACH, R. 2003 The geoflow-experiment on ISS (part II): numerical simulation. *Adv. Space Res.* **32** (2), 181–189.

TRAVNIKOV, V., SZABO, P.S.B., GAILLARD, Y. & EGBERS, C. 2025 Centrifugally driven spherical gap convection with polar angle-dependent boundary condition: can the Nusselt number fall below unity? *Phys. Fluids* **37**, 083618.

TRAVNIKOV, V., ZAUSSINGER, F., HAUN, P. & EGBERS, C. 2020 Influence of dielectrical heating on convective flow in a radial force field. *Phys. Rev. E* **101** (5), 053106.

https://doi.org/10.1017/jfm.2026.12105 Published online by Cambridge University Press

TRITTON, D.J. 1975 Internally heated convection in the atmosphere of Venus and in the laboratory. *Nature* **257** (5522), 110–112.

TRITTON, D.J. 1977 *Physical Fluid Dynamics*. Springer Netherlands.

TROWBRIDGE, A.J., MELOSH, H.J., STECKLOFF, J.K. & FREED, A.M. 2016 Vigorous convection as the explanation for Pluto's polygonal terrain. *Nature* **534** (7605), 79–81.

TURNBULL, R.J. 1968 Electroconvective instability with a stabilizing temperature gradient. II. Experimental results. *Phys. Fluids* **11** (12), 2597–2603.

TURNBULL, R.J. 1969 Effect of dielectrophoretic forces on the Bénard instability. *Phys. Fluids* **12** (9), 1809–1815.

VILELLA, K., LIMARE, A., JAUPART, C., FARNETANI, C.G., FOUREL, L. & KAMINSKI, E. 2018 Fundamentals of laminar free convection in internally heated fluids at values of the Rayleigh–Roberts number up to 10^9. *J. Fluid Mech.* **846**, 966–998.

WANG, Q., LOHSE, D. & SHISHKINA, O. 2021 Scaling in internally heated convection: a unifying theory. *Geophys. Res. Lett.* **48** (4), e2020GL091198.

WÖRNER, M., SCHMIDT, M. & GRÖTZBACH, G. 1997 Direct numerical simulation of turbulence in an internally heated convective fluid layer and implications for statistical modelling. *J. Hydraul. Res.* **35** (6), 773–797.

YAVORSKAYA, I.M., FOMINA, N.I. & BELYAEV, Y.N. 1984 A simulation of central-symmetry convection in microgravity conditions. *Acta Astronaut.* **11** (3–4), 179–183.

YOSHIKAWA, H.N., CRUMEYROLLE, O. & MUTABAZI, I. 2013*a* Dielectrophoretic force-driven thermal convection in annular geometry. *Phys. Fluids* **25** (2), 024106.

YOSHIKAWA, H.N., KANG, C., MUTABAZI, I., ZAUSSINGER, F., HAUN, P. & EGBERS, C. 2020 Thermoelectrohydrodynamic convection in parallel plate capacitors under dielectric heating conditions. *Phys. Rev. Fluids* **5** (11), 113503.

YOSHIKAWA, H.N., TADIE FOGAING, M., CRUMEYROLLE, O. & MUTABAZI, I. 2013*b* Dielectrophoretic Rayleigh–Bénard convection under microgravity conditions. *Phys. Rev. E* **87** (4), 043003.

ZAUSSINGER, F., HAUN, P., SZABO, P.S.B., TRAVNIKOV, V., AL KAWWAS, M. & EGBERS, C. 2020 Rotating spherical gap convection in the GeoFlow International Space Station (ISS) experiment. *Phys. Rev. Fluids* **5** (6), 063502.

ZAUSSINGER, F., KREBS, A., TRAVNIKOV, V. & EGBERS, C. 2017 Recognition and tracking of convective flow patterns using Wollaston shearing interferometry. *Adv. Space Res.* **60** (6), 1327–1344.

https://doi.org/10.1017/jfm.2026.12105 Published online by Cambridge University Press